



Dense upflow fluidized bed (DUFEB) solar receivers of high aspect ratio: Different fluidization modes through inserting bubble rupture promoters

Yimin Deng, Florian Sabatier, Raf Dewil, Gilles Flamant, Alex Le Gal, Ronny Gueguen, Jan Baeyens, Shuo Li, Renaud Ansart

► To cite this version:

Yimin Deng, Florian Sabatier, Raf Dewil, Gilles Flamant, Alex Le Gal, et al.. Dense upflow fluidized bed (DUFEB) solar receivers of high aspect ratio: Different fluidization modes through inserting bubble rupture promoters. Chemical Engineering Journal, 2021, 418, pp.129376. 10.1016/j.cej.2021.129376 . hal-03187264

HAL Id: hal-03187264

<https://hal.science/hal-03187264>

Submitted on 23 Oct 2023

HAL is a multi-disciplinary open access archive for the deposit and dissemination of scientific research documents, whether they are published or not. The documents may come from teaching and research institutions in France or abroad, or from public or private research centers.

L'archive ouverte pluridisciplinaire **HAL**, est destinée au dépôt et à la diffusion de documents scientifiques de niveau recherche, publiés ou non, émanant des établissements d'enseignement et de recherche français ou étrangers, des laboratoires publics ou privés.





Open Archive Toulouse Archive Ouverte (OATAO)

OATAO is an open access repository that collects the work of Toulouse researchers and makes it freely available over the web where possible

This is an author's version published in: <http://oatao.univ-toulouse.fr/27687>

Official URL: <https://doi.org/10.1016/j.cej.2021.129376>

To cite this version:

Deng, Yimin and Sabatier, Florian  and Dewil, Raf and Flamant, Gilles and Le Gal, Alex and Gueguen, Ronny and Baeyens, Jan and Shuo, Li and Ansart, Renaud  *Dense upflow fluidized bed (DUFB) solar receivers of high aspect ratio: Different fluidization modes through inserting bubble rupture promoters.* (In Press: 2021) Chemical Engineering Journal, 418. 129376. ISSN 1385-8947

Any correspondence concerning this service should be sent
to the repository administrator: tech-oatao@listes-diff.inp-toulouse.fr

Dense upflow fluidized bed (DUFb) solar receivers of high aspect ratio: Different fluidization modes through inserting bubble rupture promoters

Yimin Deng^{a,b,1}, Florian Sabatier^{c,1}, Raf Dewil^a, Gilles Flamant^{d,e}, Alex Le Gal^{d,e}, Ronny Gueguen^{d,e}, Jan Baeyens^{b,*}, Shuo Li^b, Renaud Ansart^{c,*}

^a KU Leuven, Department of Chemical Engineering, Process and Environmental Technology Lab, 2860 Sint-Katelijne-Waver, Belgium

^b Beijing University of Chemical Technology, Beijing Advanced Innovation Centre of Soft Matter Science and Engineering, Beijing, Chaoyang District, 100029, China

^c Laboratoire de Génie Chimique, Université de Toulouse, CNRS, INPT, UPS, Toulouse, France

^d PROMES-CNRS, Route du Four Solaire, 7, 66120 Font-Romeu-Odeillo-Via, France

^e Laboratory PROMES-CNRS, University of Perpignan (UPVD), Tecnosud, Rambla de la Thermodynamique, 66100 Perpignan, France

A B S T R A C T

Keywords:

Particle-in-tube solar receivers
Bubble rupture promoters
Fluidization regimes
CFD simulation
Two Fluid Model and sub-grid model
Gas through flow

A fluidized bed of Geldart-A particles is promoted as heat transfer fluid in the tubular solar receivers of solar towers. A pressure-driven upward particle flow affects the hydrodynamic flow structure and properties of the fluidized bed. Experiments involved a tube of 0.05 m internal diameter but of very high height/diameter ratio (>120), representative of the future solar receiver and of numerous chemical reactors. Solid circulation fluxes and aeration velocities were varied. Configurations of a bare tube and a tube with bubble rupture promoters were compared. In the bare tube, freely bubbling is transformed into axi-symmetric slugging at a bed level of ~ 1 m. With bubble rupture promoters, freely bubbling prevails to about a bed level of 3 m, and a turbulent fluidization mode develops higher up the tube (a more chaotic two-phase system with elongated and unstable “gas voids” and “dense solid clusters”), without axi-symmetric slugging detected. Experimental results for both tube configurations were assessed and compared with CFD predictions by the Euler n-fluid code, NEPTUNE_CFD. A good agreement of bed properties was obtained for slug/void frequencies and solids volume fraction in both tube configurations. BRPs moreover enhance the bubble through flow of the fluidizing gas, thus limiting the visible bubble flow rate and bubble sizes while increasing the gas/particle contact, and hence important in designing multi-tube chemical reactors. Whereas slugging limits the heat transfer from the tube wall to the suspension at ~ 200 W/m²K, the presence of BRPs maintains a heat transfer coefficient in excess of 600 W/m²K.

1. Introduction

1.1. The development of particle-driven concentrated solar power (CSP) plants

CSP plants convert solar heat into electricity through appropriate thermodynamic cycles. Heliostats concentrate solar radiation onto a solar receiver, where the solar heat is absorbed and transferred to a heat transfer fluid (HTF). Solar heat can hence be stored before being converted to electricity in a steam or gas turbine, while enabling CSP plants to supply electricity on demand during peaks, replacing back-up fossil fuels to ramp up the electricity production when demanded by the grid. In the current state-of-the-art central receiver solar towers, molten salts

are used as HTF and thermal energy storage (TES) medium. This solution is efficient but the minimum (260 °C) and maximum (600 °C) operation temperatures are limited by salt solidification and chemical degradation respectively [1–3]. These limitations are avoided by substituting current molten salts (mostly eutectic Na and K nitrates) by alternative HTFs with a special attention paid to using high pressure gas, high temperature molten salts and particles [2–4].

The present study is part of the development of the particle-driven concept for future CSP power plants, where particles can be used as HTF and TES medium from ambient temperature to above 1000 °C, thus improving the thermal efficiency of the receiver, of the TES and of the thermodynamic cycles [5].

Three main particle receiver concepts are under development, i.e. the “falling particle” receiver, developed by the Sandia National

* Corresponding authors.

E-mail addresses: Baeyens.J@gmail.com, 2016880011@mail.buct.edu.cn (J. Baeyens).

¹ Considered equally as principal authors.

Nomenclature

Symbols

A	Cross-sectional area, m^2
Ar	Archimedes number, –
d_B	Frontal diameter of bubble, m
d_{sv}	Surface/volume mean diameter of powders, m or μm
f_{as}	Theoretical axi-symmetric slugging frequency, s^{-1}
f_{ws}	Theoretical wall-slugging frequency, s^{-1}
g	Gravitational constant, 9.81 m s^{-2}
G_s	Solid upward flux, $\text{kg m}^{-2}\text{s}^{-1}$
H	Fluidized bed height, or level in the bed, m
N	cross sectional bubble/slug frequency, $\text{s}^{-1} \text{ m}^{-2}$
Re	Reynolds number, –
U	superficial gas velocity, m s^{-1}
U_c	Velocity at which the amplitude of pressure fluctuations across the bed reached a maximum, m/s
U_k	Velocity at which the amplitude of these fluctuations leveled off after falling from the maximum, m/s
U_{mb}	Superficial gas velocity at minimum bubbling, m s^{-1}
U_{mf}	Superficial gas velocity at minimum fluidization, m s^{-1}
U_{pt}	Onset superficial gas velocity for pneumatic transport, m s^{-1}
U_{TR}	Transition gas velocity to fast fluidization velocity, m s^{-1}

Greek symbols

ΔP	Pressure drop, Pa
ΔL	Incremental bed height, m
ρ_B	Bulk density of the fluidized bed, kg m^{-3}
ρ_g, ρ_p	Density of the fluidization gas, and absolute particle density, respectively, kg m^{-3}
$\bar{\sigma}$	Standard deviation of the particle size distribution, m or μm
α_p	Solid volume fraction
γ	Bubble through flow factor
ε	Void fraction of the bed
ε_B	Fraction of total bed volume occupied by bubbles
$\varepsilon_{mf}, \varepsilon_{mb}$	Voidage of the bed at U_{mf} and U_{mb} , respectively

Abbreviations

BRP	Bubble Rupture Promoters
CSP	Concentrated Solar Power
DUFEB	Dense Upflow Fluidized Bed
EMMS	Energy Minimization Multi-Scale
HTF	Heat transfer fluid
I.D./O.D.	Internal and Outside Diameter, respectively, m
TES	Thermal Energy Storage
TFM	Two Fluid Model
UBFB	Upflow Bubbling Fluidized Bed

Laboratories (SNL, USA) [6]; the centrifugal receiver, developed by the German Aerospace Center (DLR, Germany) [7]; and finally, the particle-in-tube solar receiver (or Upflow Bubbling Fluidized Bed, UBFB), as developed by the National Center for Scientific Research, (CNRS, France) and its international partners within the European research projects “CSP-2” and “Next-CSP” [8]. Additional concepts reported in the literature include the top-irradiated fluidized bed receiver of Magaldi [9] and the top-irradiated draft tube fluidized bed of Gokon et al. [10] and Matsubara et al. [11]. The experimental research covered ambient and on-sun single tube receivers of small internal diameter I.D. and irradiated length of 1 to 2 m, single tubes of longer height (ambient conditions, up to 4 m) and ultimately on-sun solar receivers with respectively 16 or 40 parallel receiver tubes. This research and development has been presented in numerous papers, as reviewed in the Supplementary Information SI-1. The ongoing Next-CSP solar receiver involves 40 parallel tubes, each of 0.05 m I.D. and 3 m of (on-sun) irradiated height. For a further scale-up of this UBFB receiver to commercial applications of 10 to 50 MW_{th}, the multi-tube parallel operation will be applied, but tubes of taller height (preferably ≥ 6 m) are required. It was previously demonstrated that the heat transfer coefficient declines when using tubes of increasing I.D. since the particle renewal at the tube wall surface considerably diminishes [5]. Increasing the height of the tubes is the obvious solution. In the particle-in-tube solar receiver, the fluidized particles flow upward in the tube (hence called UBFB), and indirectly absorb the concentrated solar power through the tube walls. For reasons explained in section 1.2, Geldart A-particles are ideally suited for use in these receiver tubes. Olivine or cristobalite are the selected candidate HTF particles on the basis of thermal, physical, economic and environmental criteria [12]. The operation of the UBFB receiver relies upon a stable upward fluidized particle flow that can only be achieved if the transport tube is immersed in a pressurized fluidized (bottom) dispenser bed, with an injection of secondary air above the tube bottom [13]. The performance of this type of solar receiver depends on both the hydrodynamics of the particle flow, and its associated and strongly dependent wall-to-fluidized bed heat transfer coefficient that determines the sizing of the solar receiver accounting for given wall material properties [14,15]. On-sun studies in tubes of a height till 2 m, have demonstrated that heat transfer

coefficients between 800 and 1200 W/m²K are achievable for varying irradiation conditions [14–17]. Since heat transfer and solids mixing inside the receiver tube are linked, understanding the characteristics of the fluidized bed flow in long tubes of small I.D. is critical. Two flow regime transitions have been previously identified in small I.D. tubes of heights between 1 and 4 m, where bubbling and wall slugging appeared at lower bed levels ($\leq \sim 1\text{m}$), and wall slugs became axi-symmetric slugs in deeper beds [18]. Whereas the impact of wall slugs on the particle mixing is not too outspoken since they do not cover the entire cross sectional area of the tube, axi-symmetric slugs significantly hamper the heat transfer due to severely reducing the axial and radial particle mixing, and directly exposing a gas volume to contact with the tube wall, thus hampering the particle convection heat transfer [15]. It is hence important to study both the operating conditions and the possible special measures that can reduce the axi-symmetric slugging phenomena in long tubes of small I.D.

The hydrodynamic characteristics of the fluidized bed can be investigated through video imaging (in transparent tubes) and by measuring pressure gradients along the level in the bed [19,20]: a moving bubble (or slug, or gas void) creates a positive pressure at its top, and a negative suction pressure in its wake. When such gas-filled entity hence moves within the measuring field of a pressure probe, it results in a positive pressure peak followed by a negative dip of the pressure signal. This signal can be analyzed by time-dependent and frequency treatments, giving information not only on the flow dynamics (velocity, frequency and size, among others), but also on the overall flow regime [21–23]. A sudden change of these parameters in function of mostly level within the tube, corresponds to a change of the flow regime and transitions between the fluidization modes can be distinguished. These measuring techniques will be used to meet the objectives of the research, as detailed in section 1.4.

1.2. Fluidizing Geldart A-particles

Geldart [24] classified the gas fluidization behavior of particles in Cohesive, Aeratable, Bubbling and Different (coarse) groups. Appropriate equations to delineate the particle class boundaries were developed with the average particle size, d_{sv} , and gas/solid densities, ρ_g and ρ_s

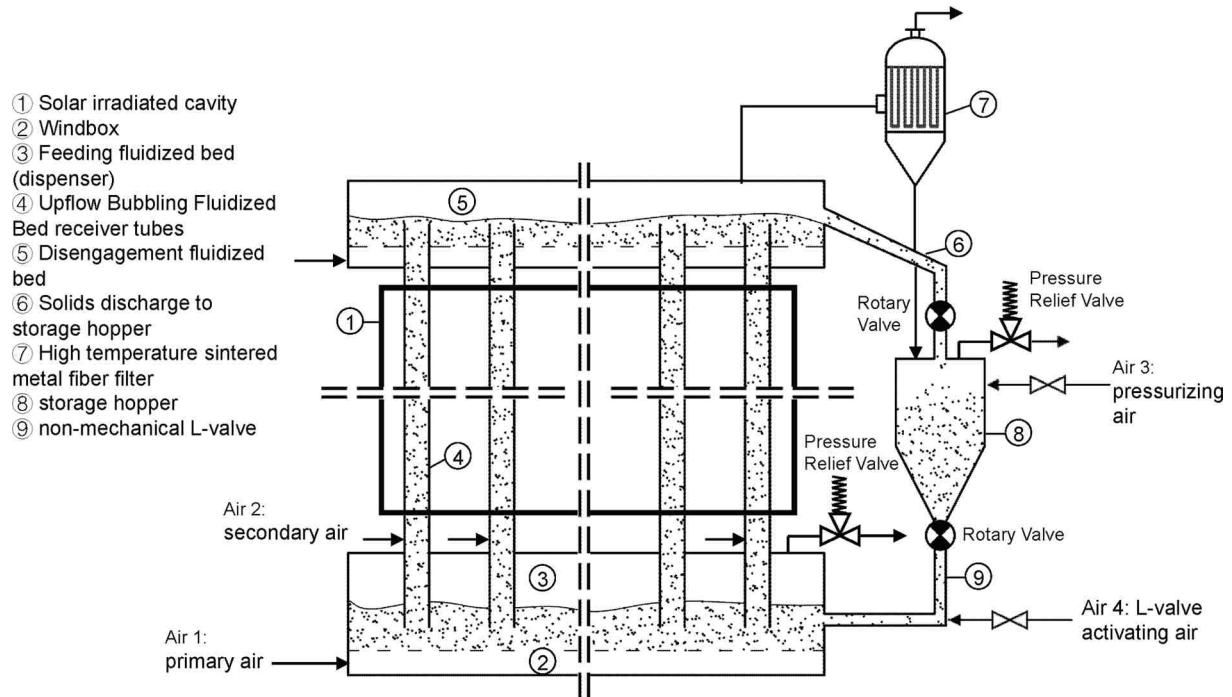


Fig. 1. Solar receiver with multi-parallel receiver tubes of small I.D. and tall height.

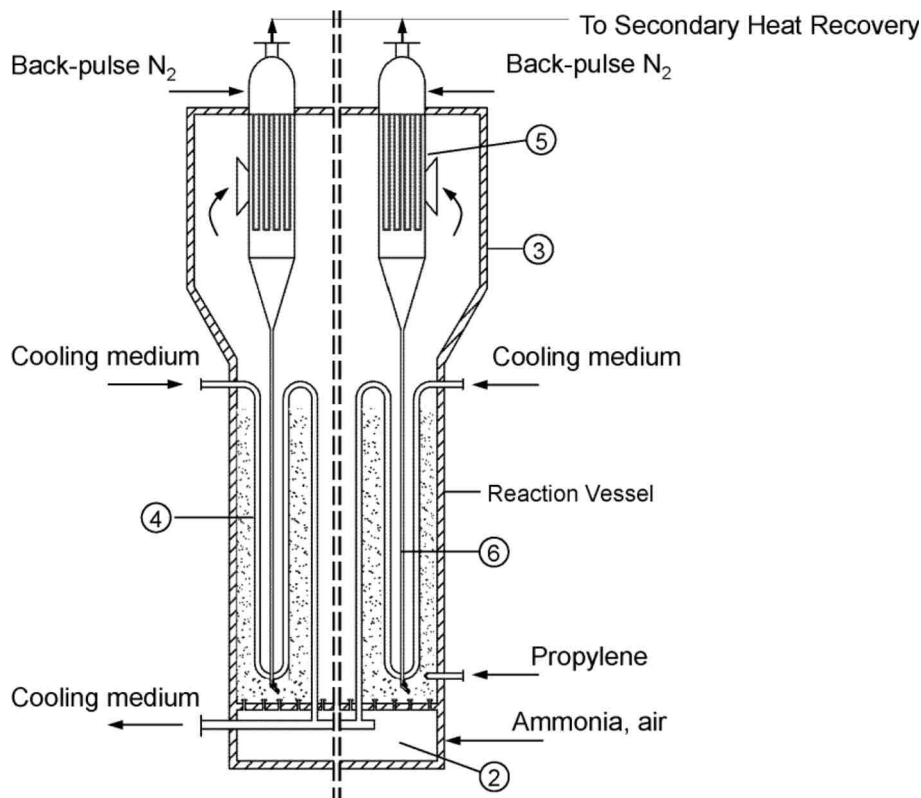


Fig. 2. Illustration of the Acrylonitrile reactor with multi-tube heat exchanger.

as main parameters [18]. The present study uses Geldart-A cristobalite silica with absolute density $\rho_s \sim 2800 \text{ kg/m}^3$. Geldart-A particles in the range of 30 to 80 μm offer hydrodynamic advantages. Geldart-B (80 to 440 μm) and Geldart-D particles ($\geq 450 \mu\text{m}$) complete the particle classification but are not suitable for the upflow bubbling receiver tube application, mostly due to the reduced particle mixing and lower heat

transfer coefficient obtained [5,15].

Geldart-A powders, widely applied in commercial gas/catalytic fluidized bed reactors [25], were proven to open new perspectives in solar receivers [5,14]. Their behavior has been studied in detail [18,24,26,27]: they are easy to handle and to convey, while a gross circulation (similar to liquid gulf streaming [28]) and excellent particle

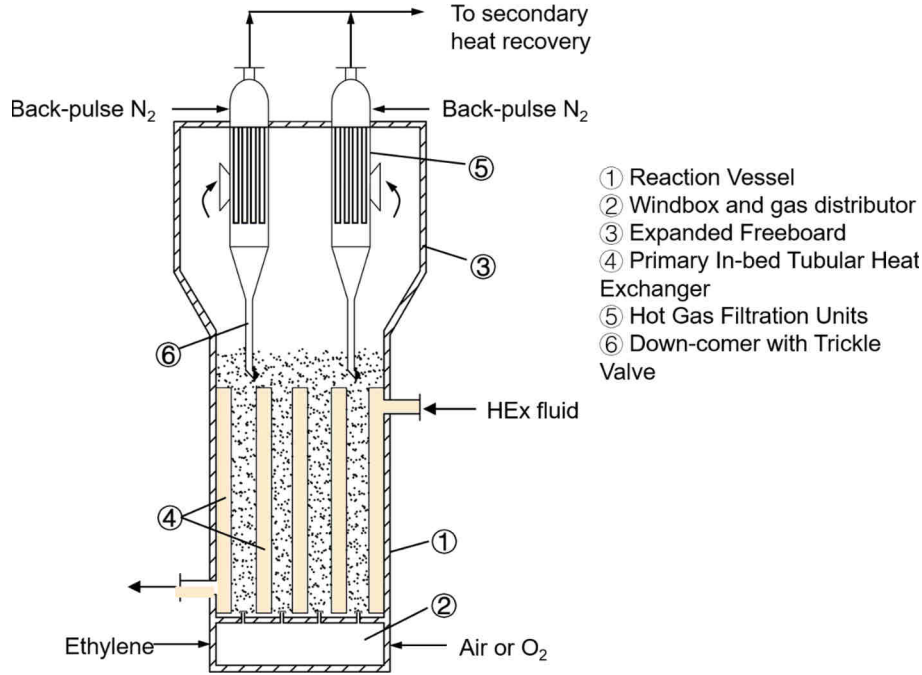


Fig. 3. Illustration of the multi-tubular reactor (e.g. production of ethylene-oxide with heat transfer to a surrounding HTF).

mixing occur in the bubbling fluidized beds. At increasing superficial gas velocities and if the bed diameter is large enough to avoid slugging [29], bubbles frequently split and re-coalesce: a maximum stable bubble size is achieved and small bubbles (<5 cm) appear to rise at a constant velocity of ~0.3 to 0.4 m/s, regardless of the bubble size, and controlled by the particle gross circulation [30]. At higher superficial gas velocities in small I.D. tubes, bubbles will transform into wall and ultimately axisymmetric slugs, with a constant frequency of about 1 and 0.5 Hz, respectively. Axi-symmetric slugs cover nearly the entire cross-section of the bed, hence reducing the axial/radial solid mixing [31].

At velocities in excess of 0.3 to 0.5 m/s, depending on the particle size, and when particle recycling is applied to maintain the bed solids' inventory, a more chaotic turbulent fluidized bed mode is achieved [32,33]. This transition will be discussed in section 1.3.

A further increase in superficial gas velocity (a few m/s) will lead to the fast fluidization mode.

Small I.D. beds are common in laboratory research, in particle-in-tube solar receivers (Fig. 1), and are hydrodynamically similar to the bed cells created by the vertical heat exchanger tubes in a commercial gas/catalytic reactor (e.g. acrylonitrile, aniline, among others [25], or in novel multi-tube ethylene oxide or vinyl acetate monomer production reactors [34]). In these exothermic reactions, multiple heat exchanging tubes are inserted in the bed, and create parallel bubbling cells, as illustrated in Fig. 2 and 3: several hundreds of tubes are inserted in the bed, limiting the free hydraulic diameter of bubbles to ≤ 0.1 m. In other exothermic applications, such as the production of ethylene oxide as illustrated in Fig. 3, the fluidized beds are really confined in multi-tubular reaction cells (of 0.05 to 0.07 m I.D.) with heat transfer achieved to the HTF surrounding these multiple tubes. In both cases, bed heights are close to 5 or 6 m. Operating conditions of these chemical reactors were reviewed by Bi et al. [35].

Clearly, the hydrodynamic study of the particle-driven solar receivers will also provide results that will be applicable to define the particle/gas behavior in these typical fluidized bed gas/catalytic reactors.

1.3. Review of fluidization regimes for group A powders

Different contacting regimes occur for varying solid/gas

characteristics, bed geometry and superficial gas velocity.

The well-known fixed bed has an increasing pressure drop with the gas flow rate, as described by the Ergun equation [36]. The equality of the drag force by the upward moving gas and the weight of the bed determines the onset of fluidization, and the superficial gas velocity at this point is the minimum fluidization velocity, U_{mf} . Above U_{mf} , the gas/solid system behaves "liquid like", with an apparent density equal to the powder bulk density. U_{mf} can be predicted by numerous empirical equations [37–39], with the equation of Baeyens and Geldart [39] used in this work for particles smaller than 100 μm .

$$U_{mf} = \frac{(\rho_p - \rho_g)^{0.934} g^{0.934} d_p^{1.8}}{1111 \mu^{0.87} \rho_g^{0.066}} \quad (1)$$

Almost all fluidization research has been performed at ambient conditions. Changing the temperature or pressure in the bed alters the properties of the gas. In A-powders, U_{mf} decreases with increasing temperature and is hardly affected by pressure. In coarser powders, U_{mf} increases with an increased temperature but is reduced when increasing the pressure. Specific correlations are available (e.g. Wu et al. [38]).

Geldart A particles [40] moreover exhibit a behavior not found in coarser solids and can be fluidized at velocities beyond U_{mf} without bubble formation until a slightly higher superficial gas velocity is reached and small bubbles appear at the surface. This higher velocity is called the minimum bubbling velocity U_{mb} [24]. Beyond U_{mf} or U_{mb} , small bubbles are formed at the distributor and grow when rising through the bed. In beds of A-particles [40], a maximum stable bubble size is reached. In beds of coarser particles, bubbles keep on growing. The fluidization regime starts to alter when the bubbles grow larger than approximately 1/3 to 1/2 of the bed diameter when wall effects determine the bubble and solids flow. The rise velocity of the bubbles, now called slugs, is determined by the bed diameter. Slugging beds are characterized by large pressure fluctuations [41].

At still higher gas velocities, approaching the particle terminal (or free fall) velocity, the two-phase (bubble/emulsion) character gradually fades out and is replaced by a condition of increasing uniformity, without large discrete bubbles and slugs, commonly referred to as the "turbulent" bed. Whereas the two-phase bubbling/slugging regime can be considered by the dense phase forming a continuous phase with gas

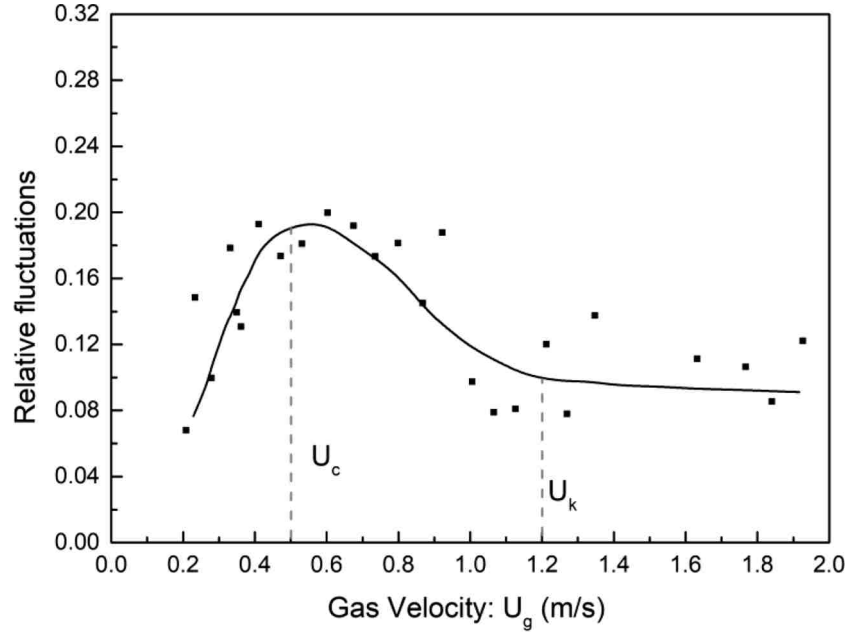


Fig. 4. U_c and U_k according to Yerushalmi (adapted from [43,44]).

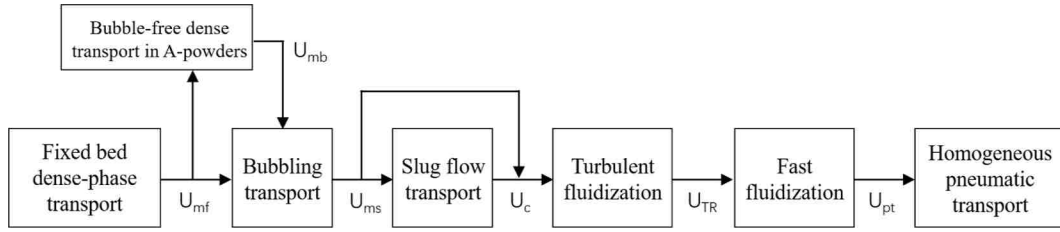


Fig. 5. Fluidization regimes for A-type particles at increasing superficial gas velocity, adapted from [52].

regions as dispersed phase, the turbulent regime covers an operation mode where gas forms the continuous phase while particle clusters constitute the dispersed phase [42,43], leading to an increasingly diffuse upper surface in the turbulent bed [44]. The transition to and characteristics of turbulent fluidization were previously assessed and described as a condition with particle clustering, with high carry-over, and with a “continuous coalescence, virtually a channeling state with tongues of fluid darting in a zig-zag fashion through the bed” [43]. Within a full range of operating velocities, Yerushalmi et al. [43] developed a fluidization diagram and fitted turbulent fluidization in between two velocities, U_c and U_k (Fig. 4). The amplitude of pressure fluctuations across the bed reached a maximum at U_c , the superficial gas velocity considered to mark the onset of turbulent fluidization. At and above U_k the ΔP fluctuations leveled off after being reduced from their maximum.

The transition occurs sharply for Geldart A powders. It is more gradual for B or D particles where the transition involves both periods of slugging and a turbulent character [43,45]. Avidan et al. [46] confirmed the turbulent regime between bubbling and fast fluidization, with the transport velocity in agreement with Yerushalmi et al. [43]. Horio et al. [47] confirmed the results of Yerushalmi et al., but demonstrated a difference between U_k and the start of the fast fluidization regime, subsequently defined as the transport velocity, U_{TR} . Perales et al. [48] and Breault and Mathur [49] found no marked difference between U_k and U_{TR} . Bubbling was seen to extinguish in the bed, but was replaced by a progressive formation of gas voids and particle clusters. Chehbouni et al. [50] demonstrated the turbulent fluidization regime between U_c and U_{TR} . Werther et al. [51] investigated the effect of the reactor scale on the turbulent fluidization regime: no significant scale effects were

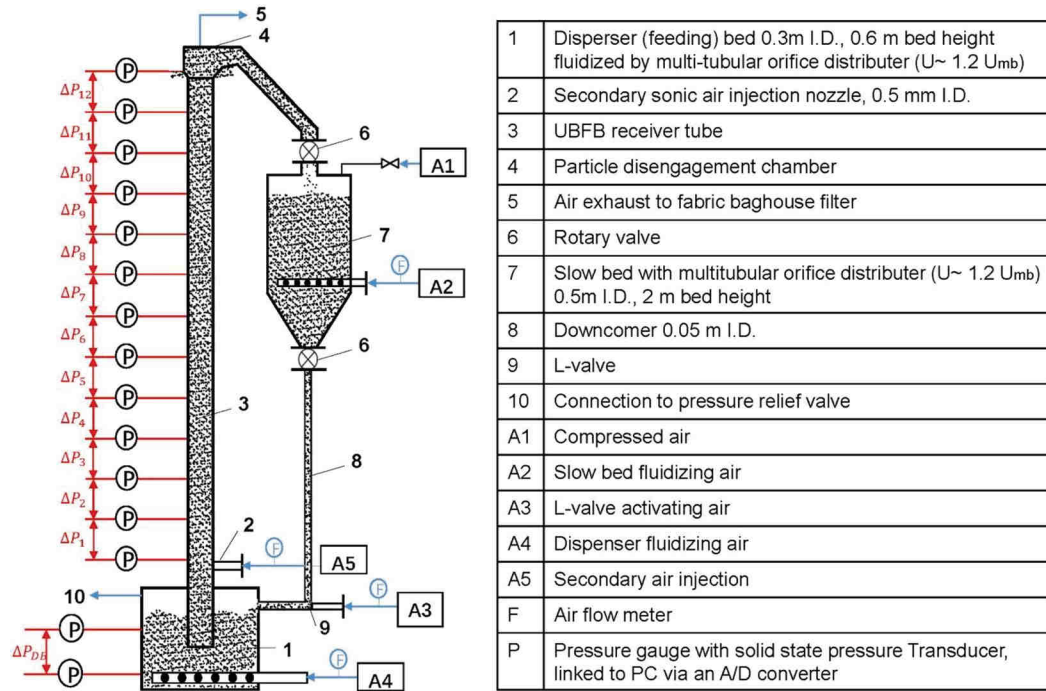
Table 1
Prediction of transition velocities.

U_{trans}	Description	Equations	Ref.
U_{mb}	Minimum bubbling velocity for A-type powders	$U_{mb} = \frac{2.07 d_p \rho_g^{0.06}}{\mu_g^{0.874}} \exp(0.716 F_{45}),$ F_{45} : fine fraction less than 45 μm	Abrahamsen and Geldart [53]
U_{mf}	Minimum fluidization velocity	$U_{mf} = \left(\frac{\mu_{air}}{\rho_{air} d_p} \right) Re_{mf} Ar = 1823 Re_{mf}^{1.07} + 21.27 Re_{mf}^2$	Wu and Baeyens [38]
U_c	Velocity at which the amplitude of pressure fluctuations across the bed reached a maximum	$U_c = \left(\frac{\mu_{air}}{\rho_{air} d_p} \right) Re_c Re_c = 0.36 Ar^{0.59}$	This work
U_{TR}	Velocity of transition to circulating fluidized bed	$U_{TR} = \left(\frac{\mu_{air}}{\rho_{air} d_p} \right) Re_{TR},$ $Re_{TR} = 3.23 + 0.23 Ar$	Zhang et al. (2015) [32]
U_{ms}	Velocity at onset of slugging	$U_{ms} = U_{mf} + 0.07 \sqrt{g D D}$: diameter of the bubbling fluidized bed	Baeyens and Geldart [41]

For Geldart A powders, these velocities will be ≤ 0.01 m/s for U_{mf} and U_{mb} ; 0.2 to 0.5 m/s for U_c ; ≥ 1 m/s for U_{TR} and in excess of 1.5 to 2 m/s for U_{pt} .

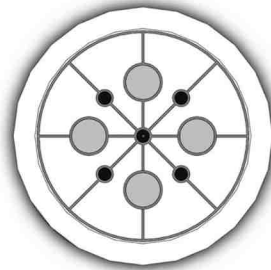
observed when progressing from bubbling to turbulent fluidization. Fast fluidization was reached when the superficial gas velocity exceeded the transport velocity, U_{TR} .

At still higher gas velocities, pneumatic conveying will occur. The

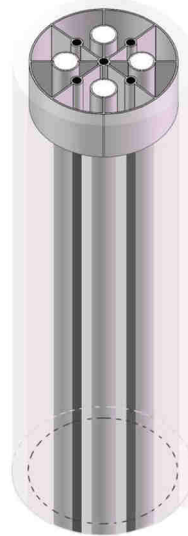


(a): General layout of the experimental rig

(a)



(b)



(b): BRP inserted into the bare tube (4 tubes of 8 mm O.D. and 5 tubes of 3 mm O.D.)

Fig. 6. (a): General layout of the experimental rig (b): BRP inserted into the bare tube (4 tubes of 8 mm O.D. and 5 tubes of 3 mm O.D.)

overall fluidization map of operation modes can be represented by Fig. 5.

Relevant transition velocities can be predicted by well-known equations. The equation for U_c was developed in the present research. All equations are given in Table 1.

1.4. Objectives

This present research was conducted at ambient temperature and focuses on the characterization of the upward suspension flow in a small

I.D. tube (0.05 m) with a large aspect ratio (height/diameter = 120), hence representative of the future commercial solar receiver set-up [54]. A cold rig was set up for several experimental campaigns with necessary particle circulation, to study the evolution of both the solid volume fraction and the flow structure. The study hence extends earlier studies, as reviewed in Supplementary Information SI-1 by (i) including the effects of solid circulation flux and aeration gas flow rates, (ii) attempting to reduce the slug formation by inserting Bubble Rupture Promoters (BRP) in the tube, resulting in a comparison of the hydrodynamic modes in a “bare tube” (BT) and in a “tube with inserted BRP” over the total

height of the tube, and (iii) assessing associated design effects of heat transfer coefficient and gas through flow. Experimental and simulation results will be used to classify the fluidization regimes.

2. Experimental

2.1. Set-up

The cold set-up consists mainly of two sections: (i) the section where particles are transported upwards, and (ii) the downward recycle section, where collected upflow particles are returned to the bottom of the set-up. The experimental rig used is shown in Fig. 6(a). The secondary sonic injection nozzle had an internal orifice diameter of 0.5 mm. Since the abatement of slug formation was considered an important target, hydrodynamic flow regimes in both the bare tube, and in a tube with inserts will be compared. These inserts, called Bubble Rupture Promoters (BRP), are illustrated in Fig. 6(b). These inserts were positioned from 0.1 m above the injection nozzle of the secondary air, and were installed throughout the height of the tube, hence till the 6 m top. Both bare and BRP tubes were experimentally investigated. The bare tube was constructed as 0.05 m I.D. polyethylene pipe, with absolute roughness coefficient of about 0.0015 mm. The BRP inserts were electro-polished stainless steel pipes with absolute roughness coefficient of about 0.0005 mm, according to ENISO 4287:1997 [55] and KEPKO [56].

Different BRP configurations with vertical tubes were initially tested (e.g. with 15 small I.D. tubes), but the configuration of Fig. 6(b) provided the best results towards bubble size reduction and transition to the turbulent fluidization mode. Earlier tests using wire mesh at different levels in the tube and even using commercial packings were proven inefficient, since they rather promoted axi-symmetric slugging.

At the exit of the upward tube, the solids are separated from the air by means of a tapered disengagement chamber of 0.3 m height, followed by a bag filter. The disengagement chamber gravitationally discharges the collected solids into the solids holding slow bed via a sealing rotary valve. For the fine particles used, it was shown that less than 2% of all circulating solids are collected in the bag filter.

The upward tube is built of three transparent polyethylene sections with an I.D. of 0.05 m, and a total height between its insert in the dispenser bed and the disengagement top of 6.6 m. The height of the tube was 5.9 m above the level of the secondary air injection. The whole rig was electrically grounded to minimise electrostatic effects. The dispenser (feeding bed) has an I.D. of 0.3 m, a total height of 0.7 m and a fluidized bed height of 0.55 to 0.6 m. The superficial fluidization velocity was $1.2 U_{mb}$ in the dispenser. The dispenser is fitted with a multi-tubular (4 tubes) and multi orifice (0.5 mm I.D) distributor with a pressure drop of 1550 Pa at a superficial air velocity of 0.01 m/s, thus considerably exceeding the design values for common distributors [57]. The dispenser was pressurized to about 1.7 bar and excess air was bled off through a pressure relief valve [13,18,58].

The major part of the in-tube fluidization air was supplied by the secondary air injection, located 0.1 m above the top of the dispenser. All air flows were valve-controlled and individually monitored by calibrated digital flow meters (MF5712-N-200, Siargo). A compressor (600 NL/min), with pressure holding tank, was used to supply the air flow to the rig. The air was filtered to protect the distributors from oil or dirt.

The recycle loop feeds the separated particles to the bottom of the upward conveying tube through the bottom fluidized bed (dispenser). The fluidized bed (slow bed) in the recycle loop creates a pressure build-up, which together with the 2 rotary airlocks and the downcomer, compensates the pressure drop of the upflow tube. This slow bed of 0.5 m I.D and bed height of 2 m, was also fluidized at $1.2 U_{mb}$ through a multi-tubular, multi-orifice distributor. While in operation, the bed height in the slow bed is between 1.2 and 1.7 m. For the controlled recycle of solids to the upflow section, a rotary valve and a non-mechanical L-valve (0.05 m I.D.) were used. Both the rotary valve and L-valve were calibrated and the particle suspension flow rate could be

Table 2
Particle characteristics.

d_{50} (μm)	$\bar{\sigma}$ (μm)	ρ_p (kg m^{-3})	U_{mf} U_{mb} (cm/s)	ψ	ρ_B (kg m^{-3})	U_t (m/ s)
55.0	14.0	2800	0.34/0.53	0.64–0.71	1380	0.203

controlled to within $\pm 3\%$. The L-valve air is supplied at 0.15 m above the elbow.

2.2. Operating conditions

2.2.1. Powder used

The powder used was Geldart A-type cristobalite silica with properties as given in Table 2. The particle size distribution was measured by Malvern Mastersizer 2000. Values of the standard deviation $\bar{\sigma}$ are given in Table 2. U_{mf} and U_{mb} were measured in a separate 0.05 m I.D. fluidized bed of 1 m bed height. U_{mf} was measured from the commonly used measurement of the average ΔP at increasing and decreasing superficial air velocity, and defined as the superficial air velocity at the intersection of the sloping packed bed line and the horizontal ΔP line of the fluidized bed. U_{mb} was determined as the superficial air velocity where first bubbles were seen to erupt at the bed surface.

Values agreed with the predictions by respectively [37,38]. Particle shapes were imaged by an OPTEC DV 320 microscope, and the sphericity ψ was determined according to Cavarreta et al. [59] and Cho et al. [60]. It was revealed between 0.64 and 0.71. The packed (tapped) bulk density was 1380 kg/m^3 . U_t was calculated by the Geldart method [24]. The amount of ultrafines ($<10 \mu\text{m}$) is below 10%.

2.2.2. Measurement techniques

Three different techniques were used, two of them providing an overall qualitative picture, the other technique of pressure gradients and their fluctuations providing quantitative results. A qualitative fluidization impression is obtained from visually observing the bed surface at the top of the upward conveying tube: either the regular “piston-like” eruption pattern or a “chaotic” eruption pattern were observed. The slug eruptions were timed (frequency) and used as backing data. The second method involved using a 25 frames/second camera (Panasonic HDC-TM40) to image the two-phase behavior at different levels in the bed. The imaging technique could not provide accurate data for the bottom (bubbling) bed section due to the significant overlap of bubbles present. Measured bubble frequency results are hence liable to significant errors for the first 0.5 m in the bed.

The third method relied on the pressure gradients, measured for each 0.5 m bed level interval. All pressure probes, with a gauze on the tip to limit ingress of particles, were connected to solid state pressure transducers (Siemens) and recorded on a PC to be analyzed afterwards. Pressure gradient measurements were transformed into the mean solids volume fraction, according to Louge and Chang [61] and assuming negligible acceleration and friction effects. The solid volume fraction, α_p , is equal to $(1 - \varepsilon)$ where ε is the gas volume fraction:

$$(1 - \varepsilon) = \left(\frac{\Delta P}{\Delta L} \right) \cdot \frac{1}{\rho_p \cdot g} \quad (2)$$

To verify the conditions stipulated by Louge and Chang [61], the acceleration of the solids was calculated by the method of Rhodes and Geldart [62], while friction factors between solids and the wall in an upward transport line were calculated by the modified correlation of Konno and Saito [63].

From the calculations, the sum of the acceleration and wall-to-suspension pressure drops was below 3% of the pressure drop of the upward column and hence negligible. The pressure drop caused by bubble/slug wall friction can be calculated using a Blasius friction factor [64]. Due to the very low value of the friction factor at common bubble/slug velocity, pressure drops are of the order of a few Pascal ($\ll 1 \text{ mbar}$) only, and

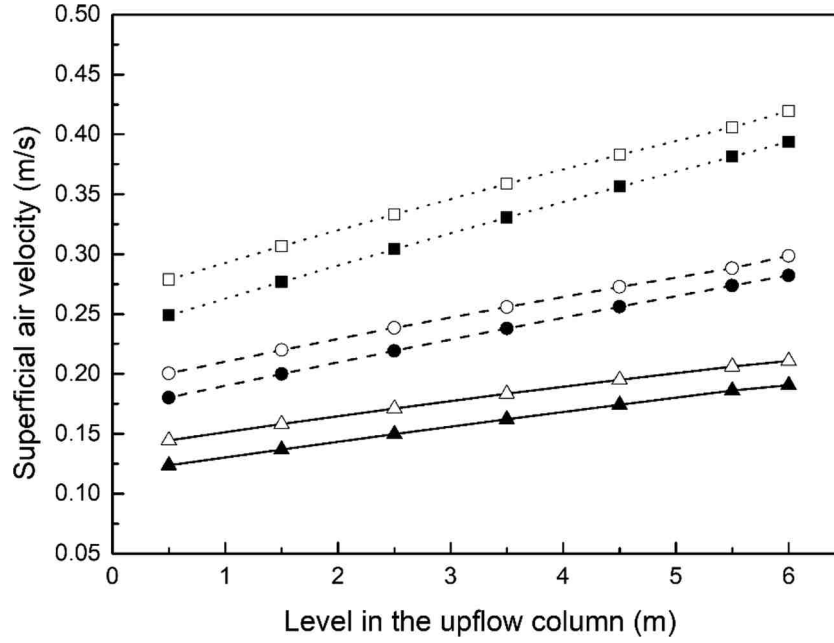


Fig. 7. Increasing superficial air velocity with level in the bed (a) Bare tube: 0.11 m/s, 0.16 m/s, 0.22 m/s (b) Tube with BRP: 0.13 m/s, 0.18 m/s, 0.25 m/s.

hence negligible in the overall pressure balance.

The influence of rising bubbles/slugs next to the pressure probes is however significant and is reflected in the pressure drop variations (Fig. 9 of section 3) where pressure increases are recorded as the bubble/slug approaches the probe, while the pressure decreases in their wakes, as previously described. Littman & Homolka [65], Xie [66] and Davidson & Harrison [67].

Equation (2) can hence be used, since acceleration and friction effects are negligible.

2.2.3. Operating conditions

The operating conditions were selected within the range of expected commercial solar receiver applications. Three superficial air flow rates were tested, and controlled at 0.11, 0.16 and 0.22 m/s (as sum of dispenser and the major secondary air injection in the bare tube). The

solid circulation fluxes were set at respectively 56 (+/- 2) kg/m²s, 105 (+/- 3) kg/m²s and 175 (+/- 6) kg/m²s, all fluxes significantly below the choking limits, as defined by Zhang et al. [68]. Due to the presence of BRP, these onset superficial velocities increased to respectively 0.13, 0.18 and 0.25 m/s in the rig due to the reduction of free cross-sectional area.

Due to the air decompression along the level in the bed, the superficial gas velocity will linearly increase towards the top of the upward column. This increased superficial air flow rate is illustrated in Fig. 7, accounting for the pressure gradients as measured, and illustrated in the section below.

After setting the air velocities in the dispenser and upflow column, the solids feeding was progressively set at the required flow rate, and stable operating conditions were seen within less than 10 min from starting the solids feeding. The solid circulation rate was checked at

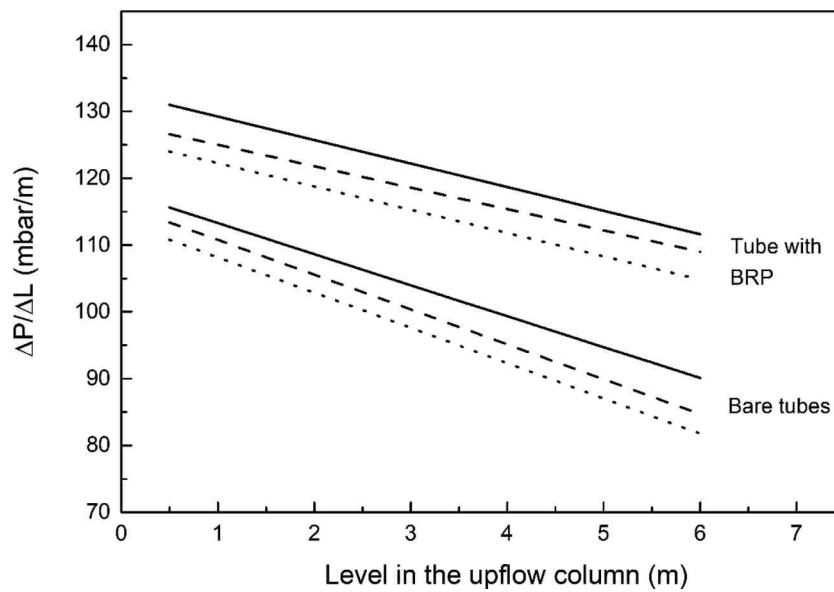


Fig. 8. Average pressure gradient versus Level in the bed, at increasing superficial air velocity, in m/s (Bare tube: -0.11 m/s, -0.16 m/s, -0.22 m/s; Tube with BRP: -0.13 m/s, -0.18 m/s, -0.25 m/s).

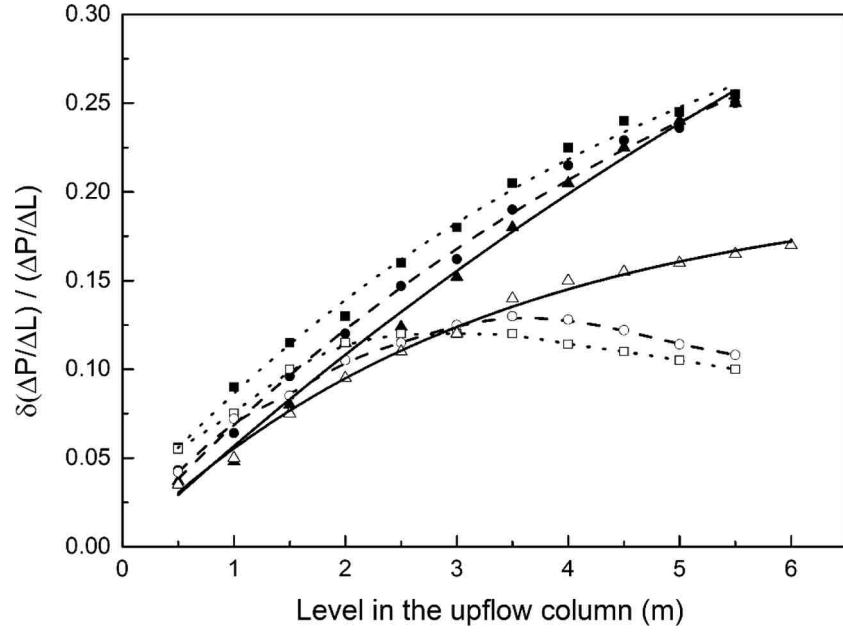


Fig. 9. Relative pressure drop fluctuations, $\delta(\Delta P) / \Delta P_{(average)}$ versus Level in the Bed, at increasing superficial air velocity, m/s (a) Bare tube: 0.11 m/s, 0.16 m/s, 0.22 m/s (b) Tube with BRP: 0.13 m/s, 0.18 m/s, 0.25 m/s.

regular intervals by measuring the time required to increase the bed level (by 3 cm) in the slow fluidized bed when stopping the rotary recycle feeding valve, and accounting for the bulk powder density at U_{mf} .

3. Experimental results and discussion

3.1. Pressure gradients and relative pressure fluctuations along the level in the upflow column

3.1.1. Bare tube versus tube with BRP

When observing the bed surface visually, differences can already be seen in both experimental conditions. In the bare tube, the bed surface at

the discharge point in the disengagement chamber remains relatively flat and rises and falls in regular 'piston-like' fluctuations, representative of a slugging fluidization mode. In the tube with BRP, the bed surface has a more turbulent appearance due to erupting chains of gas voids and trailing bubbles. In the slugging mode, the frequency of these fluctuations was easily timed and corresponded to between 0.4 and 0.5 Hz. When BRPs were present, the frequency could not be accurately defined, but exceeded 1 to 1.5 Hz.

Results obtained by the pressure probes, installed at a 0.5 m interval along the tube height, provide accurate data. The average pressure drop measured and the corresponding relative pressure drop fluctuations are given in Figs. 8 and 9. Detailed results are given in Supplementary Information S2. The signals from the pressure transducers were recorded

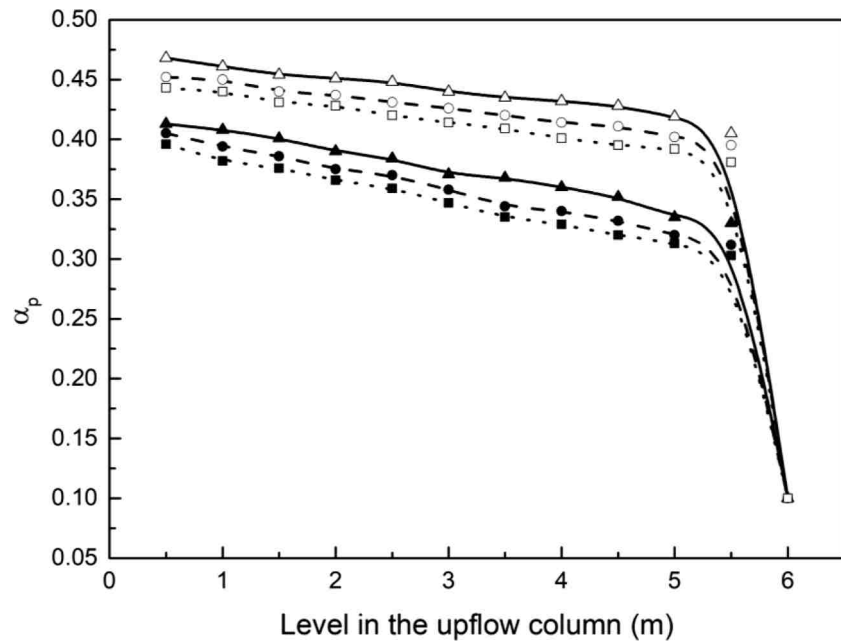


Fig. 10. Solid volume fraction versus level in the bed at increasing superficial air velocity, in m/s (a) Bare tube: 0.11 m/s, 0.16 m/s, 0.22 m/s (b) Tube with BRP: 0.13 m/s, 0.18 m/s, 0.25 m/s.

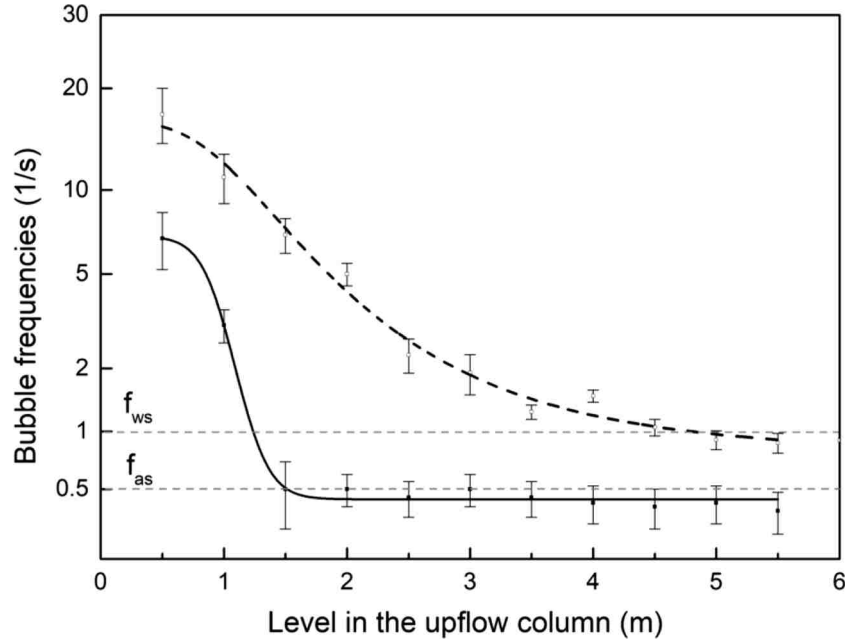


Fig. 11. Illustration of Bubble frequencies versus Level in the bed (Bare tube — ; Tube with BRP - -).

along the time of operating the experimental set-up at the different combinations of superficial air velocity and solid circulation flux. Although the average pressure gradient is given by the linear fitting of the data (Fig. 8), variations of pressures drops, expressed as the ratio of the fluctuations $\delta(\Delta P)$ and the average pressure drop ΔP , are represented in Fig. 9.

Pressure fluctuations increase with the level of measurement in the bed, although a difference between the bare tube and the tube with BRP is clearly seen. In the bare tube experiments, the fluctuations increase almost linearly with the level in the bed and the very large pressure fluctuations (up to 25%) are caused by the occurring slugs. Axis-symmetric slugging was evident over the entire height in the bare tube, with pressure fluctuations exceeding 10% of the pressure gradient at the given air velocities, in line with the rule of thumb stated by Leva [69]. The magnitude of the pressure fluctuations increased with air flow rate and with the level in the bed.

For the tube with BRP, axis-symmetric slugs were not observed, and rising bubbles transformed rapidly into turbulent voids. Relative pressure fluctuations were moreover seen to level off from a 2 to 3 m level in the bed, except for the lowest air flow rate and solid circulation flux, where the fluctuations continue to increase albeit at a lesser extent than measured in the bare tube. In accordance with the treatment of the flow modes in section 1.2 [39,40], a turbulent fluidization mode is achieved in the tube with BRP. The axis-symmetric slug mode of the bare tube is not reached. Imaging moreover revealed that the turbulent voids swirl around the BRP.

3.2. Solid volume fraction

The solid volume fraction was derived from the pressure gradient measurements according to Eq. (2): $\Delta P = \alpha_p \rho_p g \Delta L$. Fig. 10 indicates that the averaged particle volume fraction α_p ranges from 0.30 to 0.42 for the bare tube experiments. The same figure illustrates that an increasing aeration flow rate reduces the values of α_p . For the tube with BRP, α_p values are about 10% higher at an equivalent level in the bed, which implies a lower bubble fraction in the bed, as discussed in section 5.1.

3.3. Bubbling/Slugging/Turbulent characteristics in the bare tube and BRP operation mode

Fig. 11 illustrates the frequency data obtained in both experimental rigs at conditions of 0.16 m/s (bare tube) and 0.18 m/s (BRP) at a solid flux of 105 kg/m²s. Similar data were obtained for the other experimental conditions, even with very similar values of frequencies in the bubbling section of the tubes. Whereas data at low levels in the bed are tentative only (due to the very high degree of bubbling at lower bed levels in both cases), pressure fluctuations can more readily be interpreted at levels above 1 m, and decrease with the level in the bed to about 0.4 Hz (bare tube) and 0.9 to 1.5 Hz (BRP).

The frequency of ~ 0.4 Hz corresponds with the theoretical value for an axis-symmetrically slugging, f_{as} [18,23]. The theoretical frequency limit for wall-slugging, f_{ws} , is also indicated and should be ~ 1 Hz. In turbulent fluidization, frequencies even exceed the wall-slugging values.

Close to the disengagement (from 5 to 6 m), “voids” elongate and burst.

In the bare tube operation, Fig. 11 determines the transition level from bubbling to slugging at 1–1.5 m above the secondary aeration. For the BRP operation, bubble/void frequencies remain higher and axis-symmetric slugging is not obtained.

4. Simulation of the hydrodynamics by NEPTUNE_CFD code

4.1. Simulation principles

Several numerical simulation approaches can be applied to gas-particle fluidized beds. The Euler n-fluid approach, also called Two Fluid Model (TFM), is however the most efficient for the simulation of industrial scale geometries [70,71].

The capabilities of the TFMs are proven to accurately reproduce the flow behavior of gas-fluidized beds of Geldart B particles [71]. However, dealing with ultrafine Geldart A particles remains a challenge. Due to computational limitations, the practical number of cells useable for the discretization of a 3D industrial geometry of several meters in size is limited. Consequently, such systems can only be solved on coarse meshes, which are unable to fully resolve the flow meso-structures and results in a large overestimation of the bed expansion [72–74]. For instance, in the recent work of Sabatier et al. [23], the use of a cell size of

at least twice the particle diameter is recommended to accurately predict the transition from bubbling to slugging, resulting in more than 10^9 cells in the case studied here.

On a more general basis, computational analyses of the relative weights of the various terms involved into the particle momentum balance equation established that for numerical simulations of Geldart A particles in dense fluidized beds, the gravitational term and the drag term are prevailing whereas the particle phase stress plays a secondary role [75,76].

Therefore, as a first approach towards the integration of the effects of unresolved structures, McKeen et al. [77] proposed to reduce the over-estimated drag force in homogeneous fluidization by an empirical factor. This approximation can be considered as determining the drag for a characteristic length of an effective particle agglomerate diameter rather than for a single particle.

This scaling factor was used by Venier et al. [54] in numerical simulation for similar particles fluidized in a vertical tube of 5 cm I.D. for an expanded bubbling fluidized bed height of about 1 m.

Wang [78] however pointed out that this scaling factor not only depends upon the properties of the studied suspension but also on specific simulation conditions to include particles and gas physical properties, fluidization velocity, reactor geometry, grid size, among others.

A more refined strategy consists in computing dynamically a variable scaling factor by taking into account the clustering effects as described by the Energy Minimization Multi-Scale (EMMS) model [79–85]. The EMMS approach is based on a phenomenological representation of the suspension flow as a diluted-dense dual-phase structure, thereby ensuring a good representation of mesoscopic structure effects on the interphase interactions.

Supplementing TFM with this approach, one can derive an heterogeneity index reflecting the difference between homogeneous fluidization as solved by the TFM equations within a coarse mesh, and an heterogeneous representation including the effect of unresolved meso-structures, thus allowing for a correction of the drag force as a function of local variables (voidage, slip velocity).

Drag correction in TFM simulations based on a cluster-based EMMS model has proven to significantly improve the simulations accuracy of CFB riser. More recently, this method has been extended to bubbling fluidized beds using the bubble-based EMMS approach [84,85].

It is however noteworthy that the heterogeneity index, while being a function of local variables, is specified with respect of operating conditions (physical properties of the suspension, gas superficial velocity and solid circulation flow) and requires prior knowledge of characteristic properties of the suspension in the studied fluidization regime. Consequently, it should be systematically recalculated for each application [78].

Finally, previous studies [74,76] deriving equations of a filtered TFM (i.e. where its governing equation are knowingly discretized at a spatiotemporal scale larger than the aforementioned mesoscale structures) demonstrate that its equations are similar to those of the standard TFM, with the exception that the effects of unresolved, smaller than grid size, heterogenous structures have to be considered within the constitutive laws, and thus a new set of closures has to be determined. The correlative multi-scale method, or “filtered model” [76,86–91], consider the effects of mesoscale unresolved structures on the transport equations solved in a filtered TFM coarse-grid simulation from the results of smaller scale fully-resolved simulations. Consequently, formulating higher scale phenomena by analyzing small scales mechanisms, in a process similar to Large Eddy Simulation for turbulent flows.

From a budget analysis of the filtered particle momentum equation, Parmentier et al. [76] highlighted the prevailing role of interphase interaction forces, whilst the solid stress tensor holds a secondary importance. As a result, closure models on the drag force including first-order dependence on filter size and filtered solid volume fraction demonstrated a considerable improvement over coarse-grid simulation results under a wide range of flow regimes [74,76,86–91]. To a minor

extent, the influence of additional variables upon the closure models (slip velocity) along to the consideration of closure models on the solid stress tensor are being explored [88]. Although the Parmentier et al. [76] and Ozel et al. [86] models solely depend on the filter size and the filtered solid volume fraction through a functional drag correction, a dynamic drag correction is concurrently performed, which may be considered as an implicit dependence of the model to other parameters, as discussed below. The correlative multi-scale method finally enables to simultaneously address the effect of unresolved mesoscale structures on the interphase interactions, along with the effects related to the filter spatio-temporal scale, and this regardless of the considered case. Nevertheless, it is still important to mention that this approach is solely based on the assumption that extremely refined TFM simulations can fully resolve the flow behavior.

The present simulation used the Ozel et al. [86] sub-grid model. This model is based on a two steps filtering: firstly by filtering of the drag term, and secondly the proposed approach allows to compute the parameters of the sub-grid scale model as a function of space and time [76]. This procedure has the distinct advantage of being self-calibrating and requires no a priori specification of model coefficients or the use of near-wall dependence function. This model has shown its capabilities on flows encountered in circulating fluidized beds [86] or bubbling fluidized beds [76]. However, it has never been applied to flows presenting very large bubble structures or slugs.

Transport equations are hence derived by phase assembly average for the gas phase and including the effects of the interstitial fluid through the solid phase by the kinetic theory of granular flows (KTGF) [92]. The frictional stress tensor is accounted for in the solid stress tensor through the Srivastava and Sundaresan approach [93], with an activation value for the frictional viscosity set to a solid volume fraction $\alpha_{p,min} = 0.45$ and a maximal solid compaction of $\alpha_{p,max} = 0.64$ and an angle of internal friction of $\phi = 25^\circ$.

The drag interface transfer term applies correlations of Wen and Yu [94] and Ergun [36], in function of the value of the solid volume fraction [95,96].

A laminar flow is considered as assumed in previous studies [23,97,98] and the particle random kinetic energy, q_p^2 , is integrated in a transport equation through the solid phase. All the governing equations are given in Ansart et al. [97] for the TFM, and Ozel et al. [86] for the sub-grid model. These governing equations are further detailed in the Supplementary Information SI-3.

4.2. Simulation procedure

The three-dimensional numerical simulations of the UBFB system were performed using the Two Fluid Model multiphase turbulent flow code NEPTUNE.CFD. This software has been developed for High Performance Computing [70] and was developed within the NEPTUNE project framework, rallying several partners, cited in the Acknowledgement.

The spatial discretization of the code is a 2nd order unstructured finite-volume with a centered scheme. The time integration is a 1st order fractional-step method. The algorithm core is based on an elliptic fractional time step method using iterative linear solvers or direct matrix inversion to solve all the transport equations. The time step value is imposed by the CFL and Fourier numbers. During each time step, the algorithm accounts for the density variation as a function of the pressure. The pressure is solved through a parallel multigrid solver [70].

Two 3D unstructured grids were built based on the experimental geometry of both bare and BRP tubes, as described and illustrated in Section 2, with respect of internal diameter and geometry of the BRP. Only the parts above the secondary aeration were represented, consequently limiting the simulated region of interest to vertical cylinders of 5.9 m height. The grid cells measured on average 33 particle diameters in the main flow direction and 23 particle diameters in the transverse

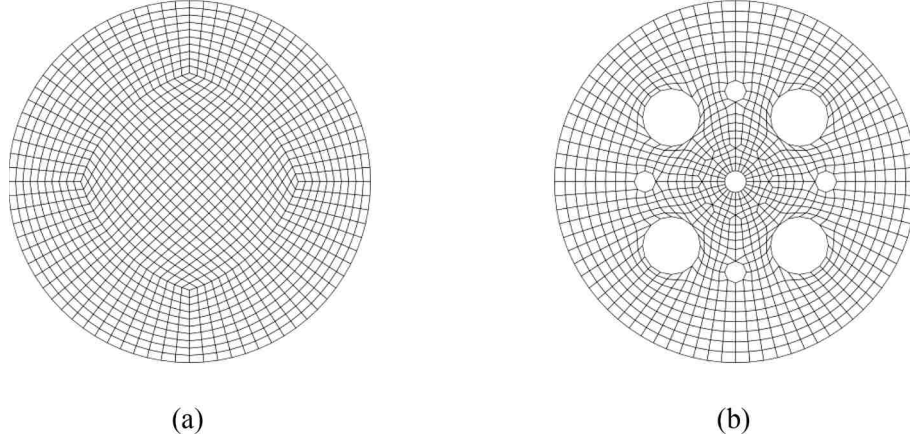


Fig. 12. . Horizontal cross-sections of the 3D meshes used for the simulation. (a) Bare tube (b) Tube with BRP.

Table 3

Phase properties and inlet boundary conditions for the simulated experimental case.

Density of air (at 293 K and 1 atm)	1.2 kg/m ³
Viscosity of air (at 293 K and 1 atm)	1.81.10 ⁻⁵ Pa.s
Absolute particle density	2800 kg/m ³
Average particle diameter	55 μm
Restitution coefficient during particle-particle collision	0.9
Solid flux at the tube bottom	105 kg/s/m ²
Inlet solid volume fraction	0.37
Superficial air velocity at the inlet	0.16 m/s

direction. The bare tube and the tube with BRP mesh consisted of 3.9 million and 3.4 million hexahedrons respectively. Fig. 12 displays horizontal cross sections of both created meshes.

Boundary conditions have been defined similarly for both

geometries. The bottom of the tube was considered as uniform mass flow inlets for both phases. Solid and gas mass flow rates were determined from the selected set of experimental operating conditions as listed in Table 3. From the experimental results, the solid fraction at the inlet was fixed at a set representative value of 0.37.

A free outlet was defined for both phases at the top of the tubes. Whereas a non-slip boundary condition was applied to the gas phase, a long and sustained particle-wall friction partial slip boundary condition was applied for the solid phase at the walls, considering elastic bouncing (with a particle-wall restitution coefficient $e_w = 1$), with a friction coefficient of $\mu_w^{pr} = 0.35$ and a zero flux condition for random kinetic energy.

In view of the importance of the height of the column for the flow behavior, the variation of the gas density due to the pressure gradient was accounted for through the perfect gas law, computing the hydrostatic pressure gradient along the tube at every iteration, which leads to

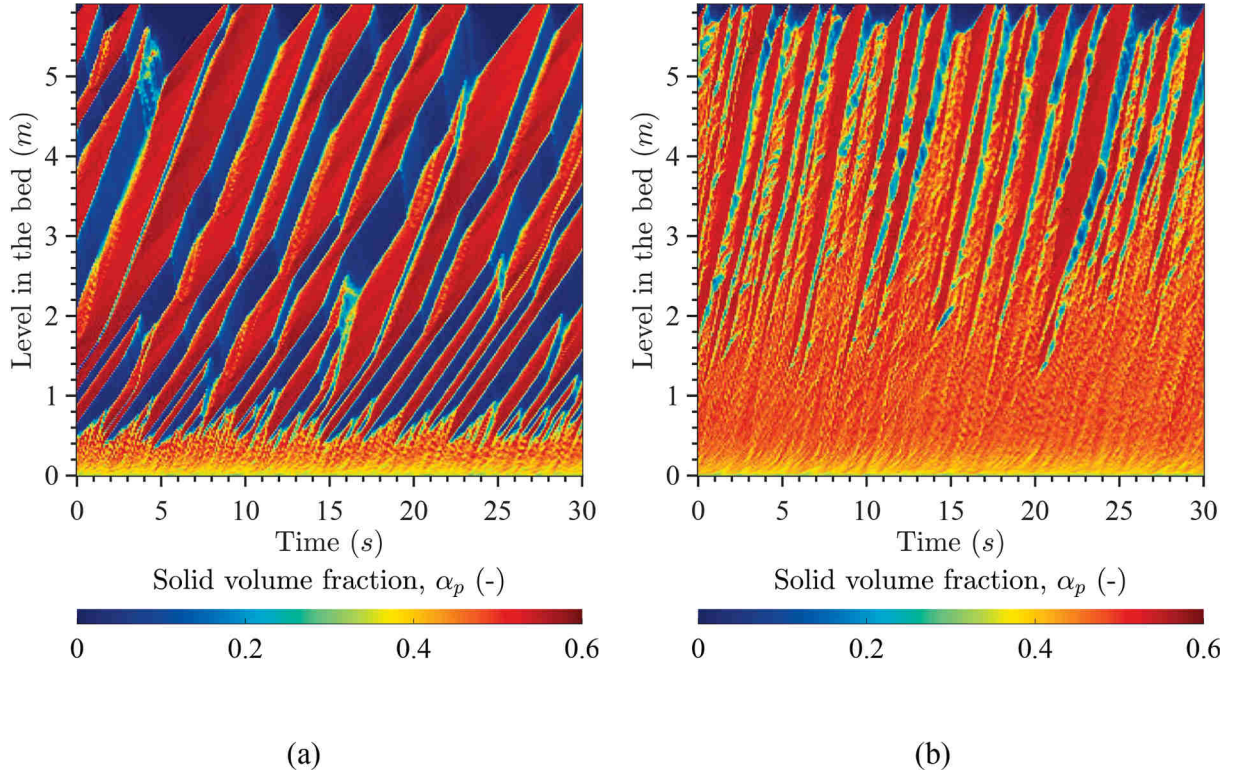
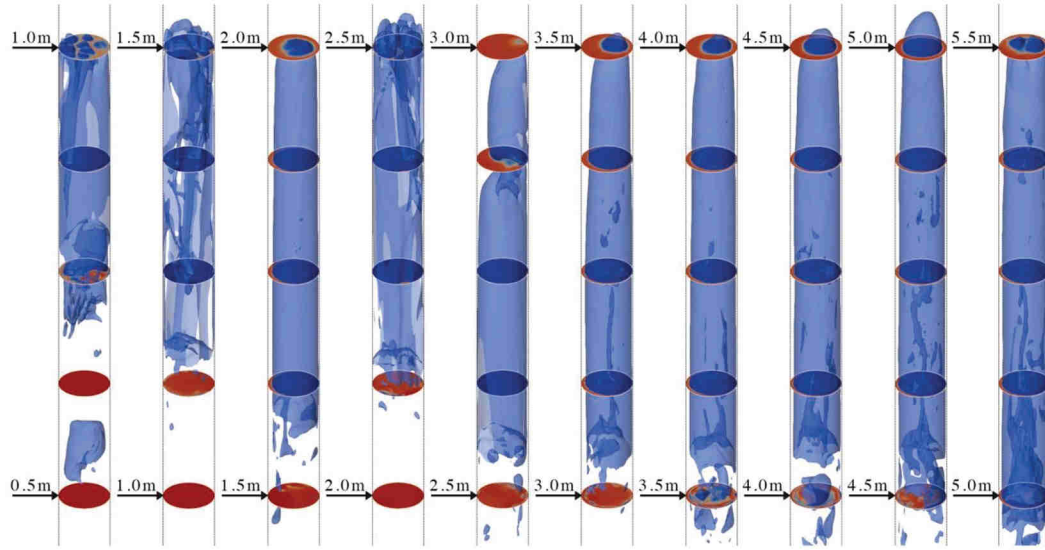
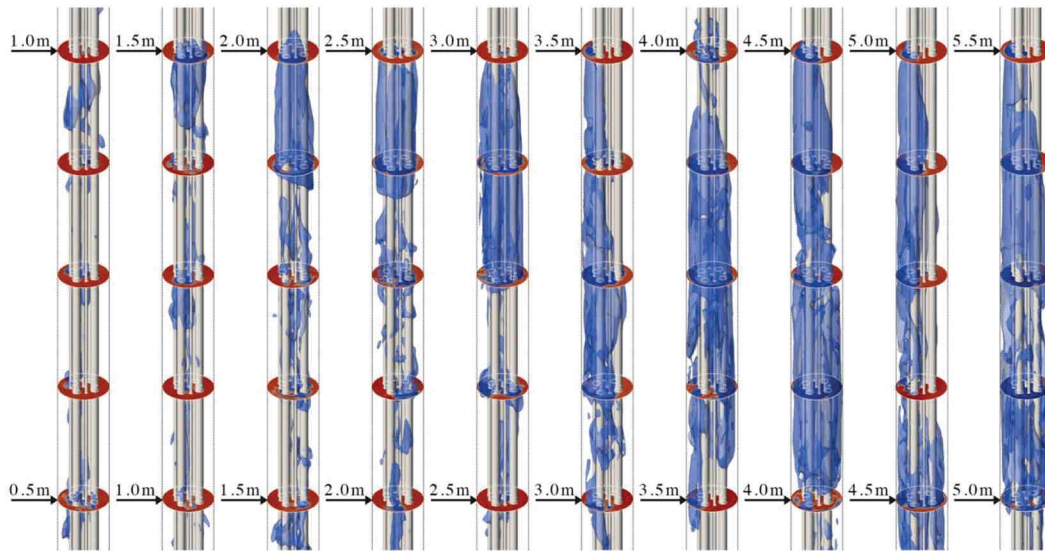


Fig. 13. Spatial-temporal evolution of the solid volume fraction averaged over horizontal slices, for (a) Bare tube, (b) Tube with BRP.



(a)



(b)

Fig. 14. Tracking of a selected slug/void during its ascent along the tube length. Bubble phase in blue, emulsion phase in red. (a) Bare tube, (b) Tube with BRP. (Additional horizontal cross sections of the solid volume fraction are displayed every 12.5 cm for reference and better depth visibility).

a significantly increasing gas velocity from the bottom to the top of the tube, i.e. in excess of 60%.

The total simulation duration for both geometries largely exceeded the duration of data sampled and studied: the total solid inventories were monitored over moving time averages to ensure that the simulated UBFBs have reached steady states. Only the last 60 s of simulations results were therefore sampled at a 10 Hz frequency and used to study the suspensions behavior.

4.3. Simulation results and discussion

Fig. 13 shows the evolution of the solid volume fraction as a function of time and space for both geometries. The vertical axis corresponds to

the vertical position within the tube and the horizontal axis to its progress with time. The values of the solid presence rate are averaged over horizontal cross-sections of about 2 mm height.

Both geometries depict a considerably different flow behavior.

In the bare tube from 0 to 50 cm, the solid volume fraction is homogeneous with a value around 45%. This flow regime is typical of a conventional bubbling fluidized bed.

Above 50 cm, the formation of oblique fringes can be identified on account of a strongly increasing fraction of the bed occupied by bubbles and thus corresponding to the transition from bubbling to slugging. From a level in the bed between 0.5 and 1.5 m, these fringes get larger and start coalescing. In this zone, wall slugs gradually merge into axisymmetric slugs.

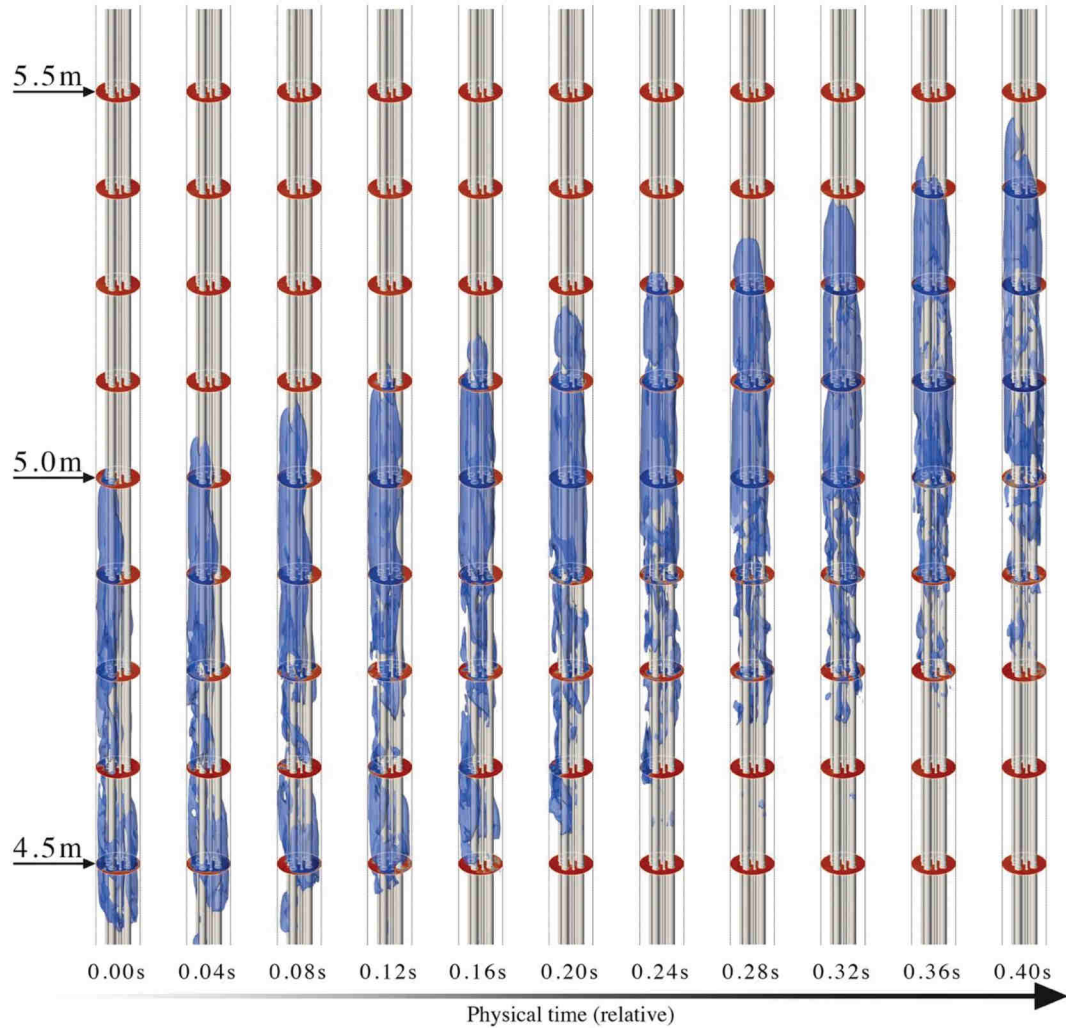


Fig. 15. Dynamic behaviour of a selected void within the tube with BRP at a level in the bed between 4.5 m and 5.5 m as a function of time. Bubble phase in blue, emulsion phase in red. (Additional horizontal cross sections of the solid volume fraction are displayed every 12.5 cm for reference and better depth visibility).

Above a bed level of 1.5 m, axi-symmetric slugs become fully developed and rise to the bed disengagement. The slope of these fringes is equal to the slug rising velocity, and a slight decrease of the slug velocity for the wall slugs, below 1 m, and the axi-symmetric slugs at higher bed levels is noticeable.

In contrast, the tube with BRP has a bubbling regime up to a level of almost 3 m. Beyond this level, fringes marking the formation of large bubble structures appear. It can be seen that the gap between dense and diluted zones is much less pronounced: diluted zones are reaching a solid presence of around 20% within a slice. Consequently, and opposed to the bare tube, these fringes are not slugs since the presence of solids inside is not zero. It can also be seen that the diluted zones length is increasing

with the bed height due to the gas decompression.

This flow regime entirely differs from the bubbling mode at the bottom of the bed and it can be related to a turbulent fluidization mode, with large gas-voids rising through the bed. The ascent velocity of these large voids is greater than that of the slugs. The BRP therefore prevented the formation of these axi-symmetric slugs.

Fig. 14 depicts the instantaneous views of a selected slug or void during its ascent along the tube length. The bubble and slug boundaries have been defined from the contour of the solid volume fraction with a threshold value of $\alpha_p = 0.20$ [99,100].

From 0.5 m to 1.5 m, the coalescence of wall slugs into axi-symmetric slugs is clearly observed in the bare tube. These slugs occupy almost the entire width of the column from this height upward, and their length is around 15 to 25 cm, in agreement with the previous 4 m high tube findings of Kong et al. [18].

In contrast, in the tube with BRP, there are smaller elongated gas voids, wrapped around the inserts and of a diameter that is limited to the space between the inserts. In the upper part of the bed, between 3 m and 5.5 m, the slugs of the bare tube occupy the entire cross-section of the tube and their length is several tens of centimeter. In the tube with inserts, the “bubble structure” of this turbulent regime is complex and chaotic: the voids are elongated, wrapped around the inserts, but never attaining very large diameters in relation to the bed section.

Fig. 15 focuses on the dynamic behavior of a selected void within the tube with BRP at a level in the bed between 4.5 m and 5.5 m. The

Table 4

Simulated void and slug characteristics for the bare tube and for the BRP tube on two slices.

Position		Bare tube	Bubble Rupture Promoters
1 m to 1.50 m	Frequency [Hz]	0.41 [0.39–0.44]	–
	Velocity [m. s ⁻¹]	0.35	–
4.50 m to 5 m	Frequency [Hz]	0.34	0.83 [0.60–1.12]
	Velocity [m. s ⁻¹]	0.49	0.9

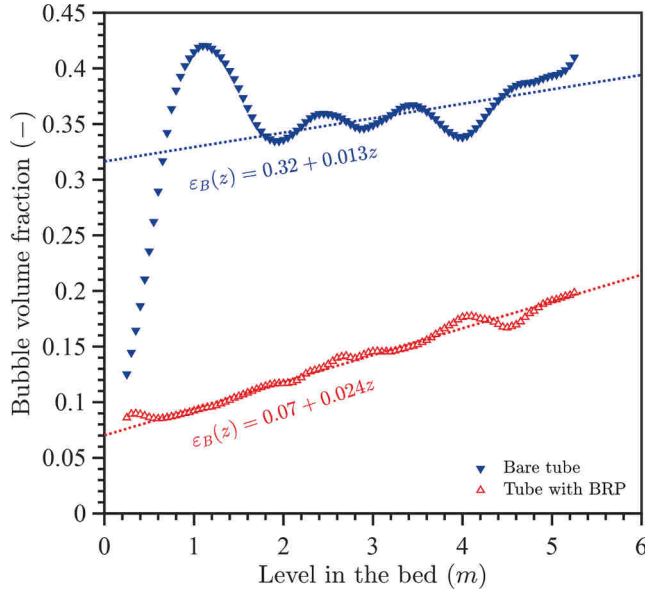


Fig. 16. Evolution of the bubble volume fraction averaged in moving slices and in time as function of the level in the bed, for both the bare tube and the tube with BRP.

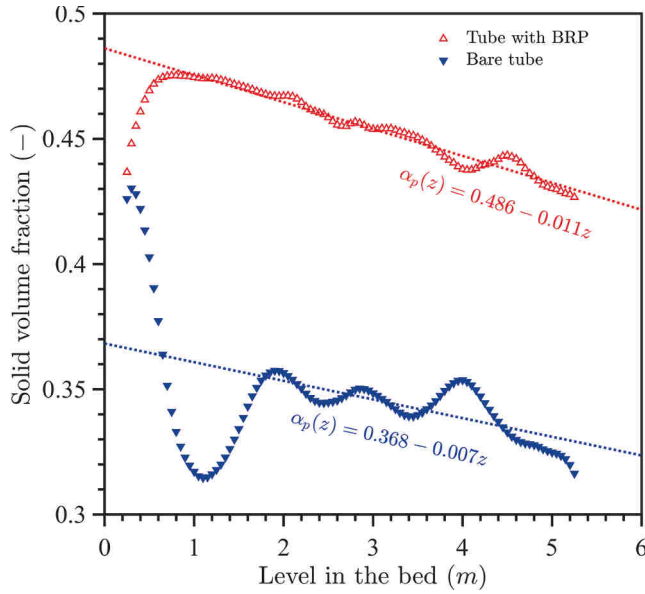


Fig. 17. Evolution of the total solid volume fraction $\alpha_p (= 1 - \epsilon)$, averaged in moving slices and in time as function of level in the bed, for both the bare tube and the tube with BRP.

bubbles boundaries are defined similarly as before.

As the void climbs up the tube, it tends to turn around itself and the inserts tubes, breaking and recombining very frequently and consequently leading to a strong agitation of the particle suspension even though a large tube section is occupied by bubbles. The phenomenon is particularly visible in the lower half of the void. Finally, to better understand the rate of breaking and recombining, it is worth noting that this figure represents the void behavior during less than a half second.

Table 4 groups the characteristics of the bubble structures' velocity and frequency computed by FFT over 60 s of sampling at 10 Hz for both the bare tube and the tube with inserts on the two bottom and top slices as defined previously. In the lower part of the bare tube, the slugs frequency is around 0.41 Hz, whereas in the upper part the axis-symmetric

slugs have a narrower natural frequency of 0.34 Hz. Due to the decompression of the gas, the velocity of these slugs increases from 0.35 m/s at the bottom to 0.49 m/s at the top of the bed.

In comparison with the experimental results of section 3, there are minor differences only. The slug frequency in the bare tube was measured at about 0.4 Hz with a rise velocity between 0.35 and 0.5 m/s. In the BRP tests, the voids' frequency could not be accurately defined, but varied between 0.9 and 1.5 Hz.

In the lower part of the tube with bubble rupture promoters, the voids frequency and velocity could not be measured precisely due to the large dispersion of the values. Between 4.5 m and 5 m, the large bubble structures have higher velocities than the slugs equal to 0.9 m/s with a relatively broad frequency range of 0.83 Hz \pm 30%. This spreading is due to the very turbulent chaotic regime induced by the presence of the inserts.

To obtain a complete insight in the average flow behavior of the suspension for the two studied tube geometries, bubble volume and solid volume fractions were computed as a function of the level in the bed (Figs. 16 and 17). Emerging tendencies for deeper beds can be linearly fitted, as illustrated in the Figures. Bottom sections (0.5 to 1.5 m) are not considered since corresponding with a freely bubbling fluidization mode, where bubbles will grow with the level in the bed and their volume fractions will increase, as shown in the Figures.

In the bare tube, from the emergence of the first slug, the volume fraction of the bubble phase is almost 33% and progressively but slowly increases further across the entire bed height: the slugging regime is well established. In this region, the total solid volume fraction slightly decreases through the level in the bed with an average value around 35%. It should be noted that these two values are in perfect agreement with the results of Kong et al. [18].

In the tube with BRP, the bubble fraction gradually increases from 5% at the bottom of the bed to 16% at a 5 m level in the bed, far below the bubble fraction within the bare tube.

The total volume fraction of solids in the BRP tube is higher than that of the bare tube. It decreases from 48% at the bottom of the bed to 45% at the top of the bed due to the strong decompression of the gas due to the pressure gradient along the tube height.

5. Impact of the experimental and simulation findings on the design and operation of small I.D and tall fluidized beds

5.1. The simulated bubble fraction and its importance in the system design

Since it was impossible to measure the bubble fraction in the system with continuous solids overflow and recycling (normally to be determined from bed expansion values), simulation results of Figs. 16 and 17 provide a clear distinction between the operation of a bare tube and a tube with BRP.

The two-phase theory of fluidization can be applied, however adapted by including a through flow factor γ [101]. According to the theory, the visible bubble flow rate, Q_B/A , is expressed in terms of the cross sectional bubble/slug frequency (N/A), the bubble volume (V_B), and the excess superficial gas flow rate ($U - U_{mf}$) as:

$$\frac{Q_B}{A} = \frac{N}{A} V_B = \gamma(U - U_{mf}) \quad (5)$$

The bubble fraction is related to the excess superficial gas flow rate and the bubble/slug velocity by:

$$\epsilon_B = \frac{\gamma(U - U_{mf})}{U_{B/S}} \quad (6)$$

The slug velocity is given by [18], with U_p as the imposed upward solid velocity (m/s).

$$U_s = 0.35\sqrt{gD} + \gamma(U - U_{mf}) + U_p \quad (7)$$

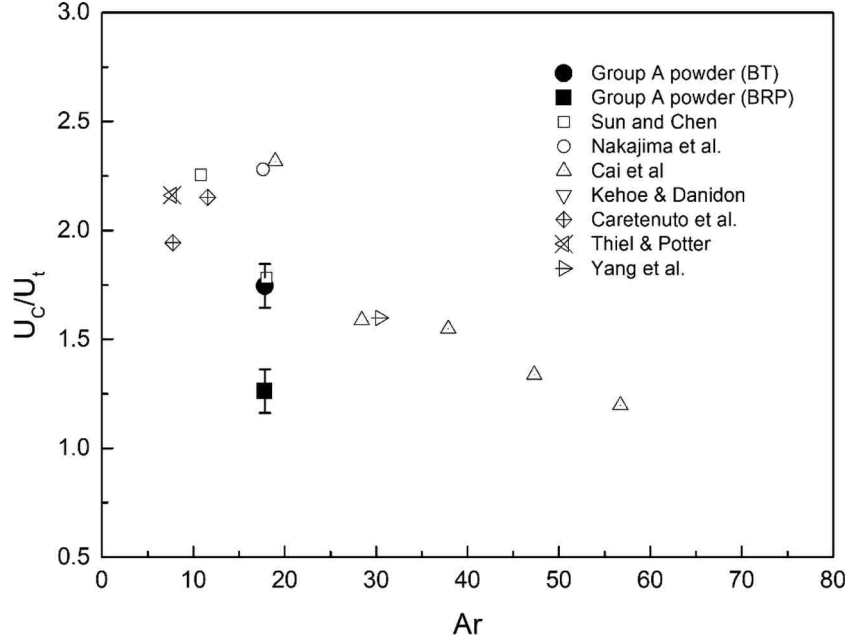


Fig. 18. Ratio U_c/U_t versus Archimedes number, Ar .

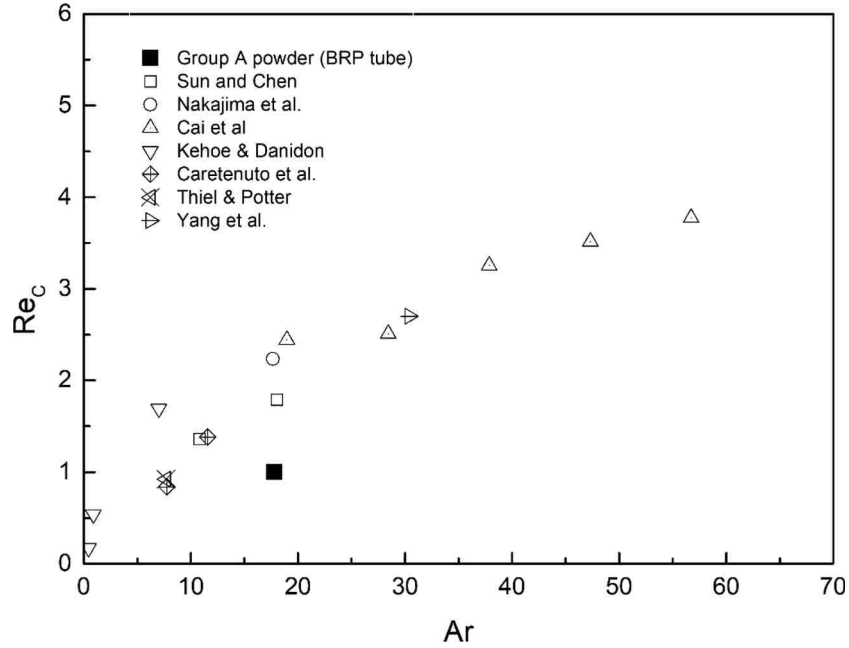


Fig. 19. Re_c versus Archimedes number, Ar .

With the values of both ε_B and U_S as determined in section 4, these equations can be applied to determine the through flow factor, γ .

For example, in the empty tube, at an average level of 4.75 m in the column, the slug velocity was 0.49 m/s and the bubble fraction was ~ 0.35 for an expanded superficial gas velocity of 0.21 m/s and an upflow solid velocity of 0.11 m/s, as determined by the solid flux and particle density. U_{mf} is very small in comparison with U , and can be neglected.

Applying the equation, with $\gamma = 0.9$ (as commonly experienced in A-type powders [100]), the calculated $U_S = 0.54$ m/s, which exceeds the predicted value (0.49 m/s) by $\sim 10\%$.

By a similar approach, the situation in the BRP experiments is completely different. The bubble fraction is ~ 0.15 for a rise velocity of

the voids of about 0.9 m/s. Due to the smaller cross sectional area by to the presence of the BRP, the corresponding superficial air velocity is 0.24 m/s at the average level of 4.75 m.

Applying Eq. (6) defines the through flow factor at $\gamma = 0.56$, meaning that a substantial part of the superficial gas velocity is by-passing the emulsion phase and flowing from void to void. This is an important finding in defining the conversions of a chemical reaction in turbulently fluidized chemical reactors, since the through flow gas will actively contact the bed catalyst and enhance the conversion in the bed of fixed bed height. The calculated rise velocity of axi-symmetric slugs by Eq. (7) with $\gamma = 0.56$ is then 0.49 m/s only, far below the predicted 0.9 m/s. According to Eq. (5), the visible bubble flow rate will be smaller than in the case of the empty tube: since the frequencies exceed the values

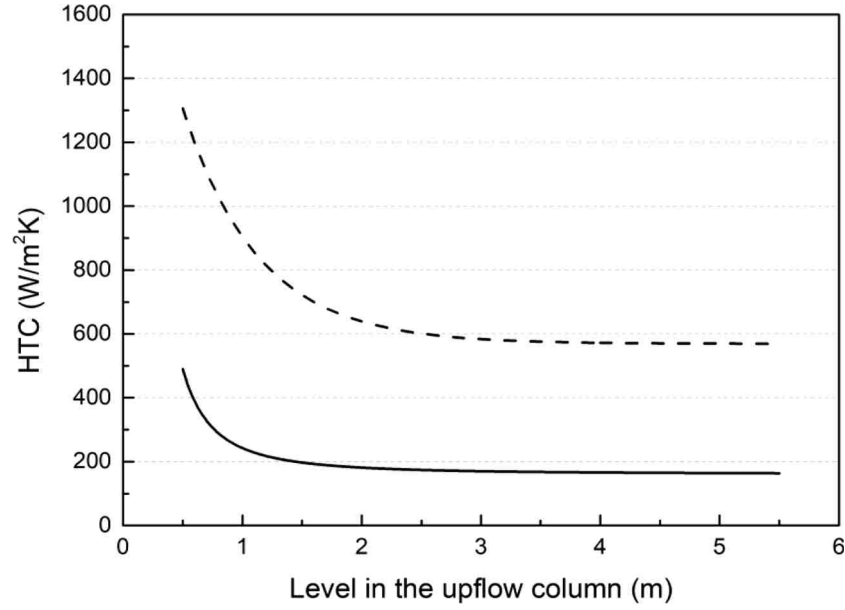


Fig. 20. Effect of operating mode on the wall-to-suspension heat transfer coefficient, as predicted by the surface renewal model [5] (Bare tube — ; Tube with BRP - -).

obtained for the empty tube slugs, the void volume must be significantly lower than the empty tube volume of the slugs obtained. The definition of an equivalent void diameter has no physical meaning, since the voids appear to be rather small in radial size, but elongated axially.

5.2. Observed transition velocity to turbulent fluidization

Literature data and experimental results concerning the velocity of transition to the turbulent fluidization regime, U_c , were gathered and transformed in either (i) the ratio of U_c and the particle terminal velocity U_t , as suggested by Yerushalmi et al. [43,44]; or (ii) the corresponding value of the Reynolds number.

The transformed results are presented in Figs. 18 and 19, respectively. Data are selected from Chen et al. [102] (also including Yang et al., Nakajima et al. and Cai et al.) and Yerushalmi et al. [43] (also providing the results of Kehoe and Davidson, Caretenuto et al., and Thiel

and Potter).

The U_c/U_t ratio increases with decreasing value of the Archimedes number, Ar . The scatter of the transformed data is most probably due to the fact that U_t was calculated, since generally not indicated in the original papers.

If transformed into Re_c , an equation could be derived for the bare tubes, as

$$Re_c = 0.36 Ar^{0.59}, (R^2 = 0.9377) \quad (8)$$

Only 1 experimental result for the tube with BRP is available. If U_c in the bare tube is 0.35 to 0.45 m/s, it is reduced to 0.2 to 0.3 m/s when BRPs are presents. Although it appears that U_c with BRP will be a fraction of the corresponding value in the bare tube, this is however based on a single data point, and should hence be considered as a tentative conclusion only. The BT data however confirm the superficial gas velocities of 0.4 to 0.5 m/s commonly applied in turbulently fluidized

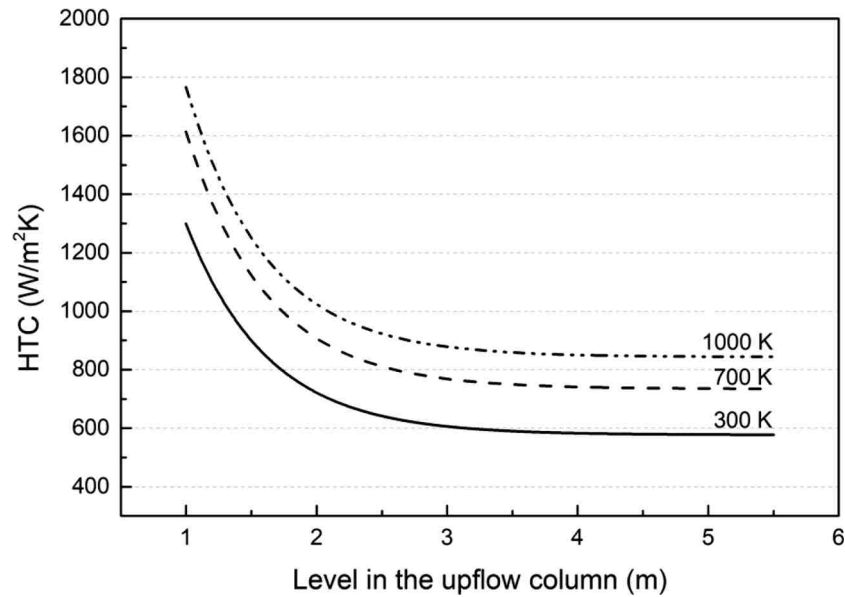


Fig. 21. Effect of the suspension temperature on the predicted heat transfer coefficient.

chemical reactors [35].

5.3. The predicted tube-wall-to-suspension heat transfer coefficient in solar receivers

Using the surface renewal model, as developed by Zhang et al. [5] for on-sun particle-in-tube experimental rigs, and with known bubble and slug characteristics (especially the renewal frequencies), the heat transfer coefficient can be predicted. Results are illustrated in Fig. 20. The effect of installing BRP in the receiver tube is significant, with the average heat transfer coefficient along the entire tube length of 6 m being at least a 3-fold of the value in the bare tube.

The heat transfer is even further increased when adding a radiation contribution, with a wall temperature of 150 °C above the suspension temperature. Predicted values for the BRP tube are represented in Fig. 21.

Although literature cites heat transfer coefficients between about 550 W/(m²K) [34] for Geldart-B particles and 800 W/(m²K) for Geldart-A particles [103,104], these values relate to the heat transfer from the bed to immersed horizontal and vertical tubes, at ambient temperature. Heat transfer from the reactor wall to the fluidized bed are however lower due to the reduced surface renewal by the particles and a reduction of ~30% has been reported [58]. The model prediction of ~600 W/(m²K) for ambient conditions seems hence very fair.

For operations in industrial chemical synthesis reactors, temperatures are between 525 and 675 K. The heat transfer coefficients will hence be close to predicted values of Fig. 21, i.e. around 800 W/(m²K) at 700 K. Since operations at higher temperature will moreover reduce the bubble sizes while increasing their frequencies, it is expected that the wall-to-bed heat transfer coefficient will be slightly further increased [5].

6. Conclusions

The present study further develops the Geldart A particles' driven technology for future Concentrated Solar Power plants, where particles are used as heat capturing and storage medium. Whereas previous investigations demonstrated that axi-symmetric slugging became a serious solid/gas hydrodynamic problem in receiver tubes of increasing aspect (height/diameter) ratio, the present investigations demonstrated that inserting bubble rupture promoters can avoid slugging and achieve a combined bubbling (bottom ~3 m of the tube) and turbulent (top ~3 m of the tube) fluidization, without axi-symmetric slugging. A receiver tube of 0.05 m I.D. and effective height of 6 m was tested, thus extending previous work, mostly limited to between 1 and 3 m high tubes.

Both the experimental results and Two Fluid Model simulations were combined to provide a better understanding of the fluidization behavior within the system. Tubes without and with bubble rupture promoters were compared for selected values of the superficial air velocity and of the imposed solid circulation flux. A very good agreement is obtained between the experimental and the simulation results in both geometries tested.

Whereas in the "bare tube" freely bubbling is transformed into axi-symmetric slugging from a level in the tube beyond 1 to 1.5 m, the bubble rupture promoters extend the freely bubbling zone to a level of ~3 m in the tube, where after a typical turbulent fluidization regime is observed, independent of the solids recycling rate. In the turbulent fluidization mode, voids are seen to break and recombine frequently, resulting in a significant through flow of gas (from void to void) and a very good heat transfer coefficient (about a threefold value of the case when axi-symmetric slugging occurs).

This very considerable through flow (45% against ~10%) is an important contribution to the design of catalytic tubular reactors, where conversions should increase due to a more extensive gas-catalyst contact than predicted by the original two-phase theory.

Further experiments and simulations are ongoing at higher operating

temperatures, where bubble sizes are predicted to be smaller and bubble frequencies increased, thus probably shifting the flow transition to higher levels in the bed, while positively affecting the wall-to-suspension heat transfer. These results will be published in a forthcoming publication.

Declaration of Competing Interest

The authors declare that they have no known competing financial interests or personal relationships that could have appeared to influence the work reported in this paper.

Acknowledgements

Authors acknowledge funding both from the European Commission through Horizon Research (H2020 grant N° 727762, project NEXT-CSP[®]) and from the Beijing Advanced Innovation Centre of Soft Matter Science and Engineering (Beijing University of Chemical Technology, China).

Authors also express their gratitude to Professor Olivier Simonin of the *Institut de Mécanique des Fluides de Toulouse (IMFT), Université de Toulouse, CNRS, Toulouse, France*, for his valuable input both into developing the gas particle filtered TFM mathematical modeling approach and into its detailed formulations as presented in Supplementary Information, SI-3.

The NEPTUNE project framework acknowledges support from the consortium EDF, CEA (Commissariat à l'Energie Atomique), IRSN (Institut de Radioprotection et de Sécurité Nucléaire), and Framatome. The modeling approach for the turbulent poly-disperse gas-solid flows was implemented by the IMFT (Institut de Mécanique des Fluides de Toulouse) and the LGC (Laboratoire de Génie Chimique). This work was performed using HPC resources from GENCI-CINES (Grant 2020-A0082B06938) and from CALMIP (Grant 2020-P1132).

References

- [1] H. Benoit, L. Spreafico, D. Gauthier, G. Flamant, Review of heat transfer fluids in tube-receivers used in concentrating solar thermal systems: Properties and heat transfer coefficients, *Renew. Sustain. Energy Rev.* 55 (2016) 298–315, <https://doi.org/10.1016/j.rser.2015.10.059>.
- [2] H. Zhang, W. Kong, T. Tan, J. Baeyens, High-efficiency concentrated solar power plants need appropriate materials for high-temperature heat capture, conveying and storage, *Energy* 139 (2017) 52–64, <https://doi.org/10.1016/j.energy.2017.07.129>.
- [3] M. Mehos, Concentrating Solar Power – Gen3 Demonstration Roadmap, n.d. REL/TP-5500-67464.
- [4] Q. Kang, R. Dewil, J. Degreve, J. Baeyens, H. Zhang, Energy analysis of a particle suspension solar combined cycle power plant, *Energy Convers. Manag.* (2018), <https://doi.org/10.1016/j.enconman.2018.02.067>.
- [5] H. Zhang, H. Benoit, D. Gauthier, J. Degreve, J. Baeyens, I.P. López, M. Hemati, G. Flamant, Particle circulation loops in solar energy capture and storage: Gas-solid flow and heat transfer considerations, *Appl. Energy* 161 (2016) 206–224, <https://doi.org/10.1016/j.apenergy.2015.10.005>.
- [6] C.K. Ho, J. Christian, J. Yellowhair, S. Jeter, M. Golob, C. Nguyen, K. Repole, S. Abdel-Khalik, N. Siegel, H. Al-Ansary, A. El-Leathy, B. Gobereit, Highlights of the high-temperature falling particle receiver project: 2012–2016, in: *AIP Conf. Proc.* (2017), 030027, <https://doi.org/10.1063/1.4984370>.
- [7] M. Ebert, L. Amsbeck, J. Rheinländer, B. Schlögl-Knothe, S. Schmitz, M. Sibum, R. Uhlig, R. Buck, Operational experience of a centrifugal particle receiver prototype, in: 2019: p. 030018. 10.1063/1.5117530.
- [8] Next-CSP project website, <http://www.next-csp.eu>, retrieved on January 15, 2021.
- [9] MAGALDI, Concentrated Solar Power STEM® – Solar Thermo-Electric Magaldi, (2020).
- [10] N. Gokon, H. Yamamoto, N. Kondo, T. Kodama, Internally circulating fluidized bed reactor using m-ZrO₂ supported NiFe₂O₄ particles for thermochemical two-step water splitting, *J. Sol. Energy Eng.* 132 (2010), <https://doi.org/10.1115/1.4001154>.
- [11] K. Matsubara, Y. Kazuma, A. Sakurai, S. Suzuki, L. Soon-Jae, T. Kodama, N. Gokon, C.H. Seok, K. Yoshida, High-temperature fluidized receiver for concentrated solar radiation by a beam-down reflector system, *Energy Procedia* 49 (2014) 447–456, <https://doi.org/10.1016/j.egypro.2014.03.048>.
- [12] Q. Kang, G. Flamant, R. Dewil, J. Baeyens, H.L. Zhang, Y.M. Deng, Particles in a circulation loop for solar energy capture and storage, *Particuology*. 43 (2019) 149–156, <https://doi.org/10.1016/j.partic.2018.01.009>.

- [13] H. Zhang, W. Kong, T. Tan, F. Gilles, J. Baeyens, Experiments support an improved model for particle transport in fluidized beds, *Sci. Rep.* 7 (2017) 10178, <https://doi.org/10.1038/s41598-017-10597-3>.
- [14] H. Benoit, I. Pérez López, D. Gauthier, J.-L. Sans, G. Flamant, On-sun demonstration of a 750 °C heat transfer fluid for concentrating solar systems: Dense particle suspension in tube, *Sol. Energy* 118 (2015) 622–633, <https://doi.org/10.1016/j.solener.2015.06.007>.
- [15] J. Baeyens, D. Geldart, Modelling approach to the effect of equipment scale on fluidised bed heat transfer data, *J. Powder Bulk Solids Technol.* 4 (1980) 1.
- [16] H. Zhang, H. Benoit, I. Perez-López, G. Flamant, T. Tan, J. Baeyens, High-efficiency solar power towers using particle suspensions as heat carrier in the receiver and in the thermal energy storage, *Renew. Energy* 111 (2017) 438–446, <https://doi.org/10.1016/j.renene.2017.03.101>.
- [17] H. Zhang, S. Li, W. Kong, G. Flamant, J. Baeyens, Scale-up considerations of the UFBF solar receiver, in: *AIP Conf. Proc.*, 2019: p. 030067. 10.1063/1.5117579.
- [18] W. Kong, T. Tan, J. Baeyens, G. Flamant, H. Zhang, Bubbling and slugging of Geldart group A powders in small diameter columns, *Ind. Eng. Chem. Res.* 56 (2017) 4136–4144, <https://doi.org/10.1021/acs.iecr.6b04798>.
- [19] J.R. Grace, J. Baeyens, Instrumentation and Experimental Techniques, in: John Wiley & Sons (Ed.), *Gas Fluid. Technol.*, Geldart D., Chichester, 1986.
- [20] M. Punčochář, J. Drahoš, Origin of pressure fluctuations in fluidized beds, *Chem. Eng. Sci.* 60 (2005) 1193–1197, <https://doi.org/10.1016/j.ces.2004.09.054>.
- [21] H.T. Bi, A critical review of the complex pressure fluctuation phenomenon in gas–solids fluidized beds, *Chem. Eng. Sci.* 62 (2007) 3473–3493, <https://doi.org/10.1016/j.ces.2006.12.092>.
- [22] F. Johnsson, R. Zijerveld, J. Schouten, C. van den Bleek, B. Leckner, Characterization of fluidization regimes by time-series analysis of pressure fluctuations, *Int. J. Multiph. Flow* 26 (2000) 663–715, [https://doi.org/10.1016/S0301-9322\(99\)00028-2](https://doi.org/10.1016/S0301-9322(99)00028-2).
- [23] F. Sabatier, R. Ansart, H. Zhang, J. Baeyens, O. Simonin, Experiments support simulations by the NEPTUNE CFD code in an Upflow Bubbling Fluidized Bed reactor, *Chem. Eng. J.* 385 (2020), 123568, <https://doi.org/10.1016/j.cej.2019.123568>.
- [24] D. Geldart, *Gas Fluidization Technology*, John Wiley, Chichester (UK), 1986.
- [25] D. Kunii, O. Levenspiel, *Fluidization Engineering*, second, Butterworth-Heinemann: Newton-MA (USA), 1991.
- [26] J. Wang, M.A. van der Hoef, J.A.M. Kuipers, CFD study of the minimum bubbling velocity of Geldart A particles in gas-fluidized beds, *Chem. Eng. Sci.* 65 (2010) 3772–3785, <https://doi.org/10.1016/j.ces.2010.03.023>.
- [27] L. Leu, F. Tsai, Hydrodynamics of Geldart group A particles in gas-solid fluidized beds, *Korean J. Chem. Eng.* 26 (2009) 513–517, <https://doi.org/10.1007/s11814-009-0087-9>.
- [28] S. Karimipour, T. Pugsley, Experimental study of the nature of gas streaming in deep fluidized beds of Geldart A particles, *Chem. Eng. J.* 162 (2010) 388–395, <https://doi.org/10.1016/j.cej.2010.05.040>.
- [29] J.M. Valverde, A. Castellanos, Bubbling suppression in fluidized beds of fine and ultrafine powders, *Part. Sci. Technol.* 26 (2008) 197–213, <https://doi.org/10.1080/02726350802026656>.
- [30] M. Ye, J. Wang, M.A. van der Hoef, J.A.M. Kuipers, Two-fluid modeling of Geldart A particles in gas-fluidized beds, *Particuology* 6 (2008) 540–548, <https://doi.org/10.1016/j.partic.2008.07.005>.
- [31] B. Du, W. Warsito, L.-S. Fan, ECT Studies of Gas–Solid Fluidized Beds of Different Diameters, *Ind. Eng. Chem. Res.* 44 (2005) 5020–5030, <https://doi.org/10.1021/ie049025n>.
- [32] H.L. Zhang, J. Degrevé, R. Dewil, J. Baeyens, Operation Diagram of Circulating Fluidized Beds (CFBs), *Procedia Eng.* 102 (2015) 1092–1103, <https://doi.org/10.1016/j.proeng.2015.01.232>.
- [33] H. Zhang, J. Degrevé, J. Baeyens, R. Dewil, The voidage in a CFB riser as function of solids flux and gas velocity, *Procedia Eng.* 102 (2015) 1112–1122, <https://doi.org/10.1016/j.proeng.2015.01.234>.
- [34] BPChemicals, BP makes Leap to VAM fluidised bed process, *Indep. Commod. Intel. Serv.* (n.d.).
- [35] H.T. Bi, N. Ellis, I.A. Abba, J.R. Grace, A state-of-the-art review of gas-solid turbulent fluidization, *Chem. Eng. Sci.* (2000), [https://doi.org/10.1016/S0009-2509\(00\)00107-X](https://doi.org/10.1016/S0009-2509(00)00107-X).
- [36] S. Ergun, Fluid flow through packed columns, *Chem. Eng. Prog.* (1952). citeulike-article-id:7797897.
- [37] J. Adánez, J.C. Abanades, Minimum fluidization velocities of fluidized-bed coal-combustion solids, *Powder Technol.* 67 (1991) 113–119, [https://doi.org/10.1016/0032-5910\(91\)80147-B](https://doi.org/10.1016/0032-5910(91)80147-B).
- [38] S.Y. Wu, J. Baeyens, Effect of operating temperature on minimum fluidization velocity, *Powder Technol.* 67 (1991) 217–220, [https://doi.org/10.1016/0032-5910\(91\)80158-F](https://doi.org/10.1016/0032-5910(91)80158-F).
- [39] D. Geldart, A.R. Abrahamsen, Fluidization of fine porous powders, *Chem. Eng. Prog. Symp.* (1981) 160.
- [40] D. Geldart, Types of gas fluidization, *Powder Technol.* 7 (1973) 285–292, [https://doi.org/10.1016/0032-5910\(73\)80037-3](https://doi.org/10.1016/0032-5910(73)80037-3).
- [41] J. Baeyens, D. Geldart, An investigation into slugging fluidized beds, *Chem. Eng. Sci.* 29 (1974) 255–265, [https://doi.org/10.1016/0009-2509\(74\)85051-7](https://doi.org/10.1016/0009-2509(74)85051-7).
- [42] J.R. Grace, J. Tuot, Theory for cluster formation in vertically conveyed suspensions of intermediate density, *Trans. Inst. Chem. Eng.* (1979).
- [43] J. Yerushalmi, N.T. Cankurt, Further studies of the regimes of fluidization, *Powder Technol.* 24 (1979) 187–205, [https://doi.org/10.1016/0032-5910\(79\)87036-9](https://doi.org/10.1016/0032-5910(79)87036-9).
- [44] J. Yerushalmi, D.H. Turner, A.M. Squires, The fast fluidized bed, *Ind. Eng. Chem. Process Des. Dev.* 15 (1976) 47–53.
- [45] C.M.H. Brereton, J.R. Grace, The transition to turbulent fluidization: Chemical reaction engineering, *Chem. Eng. Res. Des.* 70 (1992) 246–251.
- [46] A.A. Avidan, J. Yerushalmi, Bed expansion in high velocity fluidization, *Powder Technol.* 32 (1982) 223–232, [https://doi.org/10.1016/0032-5910\(82\)85024-9](https://doi.org/10.1016/0032-5910(82)85024-9).
- [47] M. Horio, H. Ishii, M. Nishimuro, On the nature of turbulent and fast fluidized beds, *Powder Technol.* 70 (1992) 229–236, [https://doi.org/10.1016/0032-5910\(92\)80058-5](https://doi.org/10.1016/0032-5910(92)80058-5).
- [48] J.F. Perales, On the transition from bubbling to fast fluidization regimes, *Circ. Fluid. Bed Technol.* (1991) 73–78.
- [49] R.W. Breault, V.K. Mathur, High-velocity fluidized-bed hydrodynamic modeling. 1. Fundamental studies of pressure drop, *Ind. Eng. Chem. Res.* 28 (1989) 684–688, <https://doi.org/10.1021/ie00090a006>.
- [50] A. Chehbouni, J. Chaouki, C. Guy, D. Klvana, Characterization of the Flow Transition between Bubbling and Turbulent Fluidization, *Ind. Eng. Chem. Res.* 33 (1994) 1889–1896, <https://doi.org/10.1021/ie00032a002>.
- [51] J. Werther, J. Wein, Expansion behavior of gas fluidized beds in the turbulent regime, *AIChE Symp. Ser.* 90 (301) (1994) 31–44.
- [52] H. Zhang, J. Baeyens, G. Cáceres, J. Degrevé, Y. Lv, Thermal energy storage: Recent developments and practical aspects, *Prog. Energy Combust. Sci.* 53 (2016) 1–40, <https://doi.org/10.1016/j.pecs.2015.10.003>.
- [53] A.R. Abrahamsen, D. Geldart, Behaviour of gas-fluidized beds of fine powders part I, Homogeneous expansion, *Powder Technol.* 26 (1980) 35–46, [https://doi.org/10.1016/0032-5910\(80\)85005-4](https://doi.org/10.1016/0032-5910(80)85005-4).
- [54] C.M. Venier, A. Reyes Urrutia, J.P. Capossio, J. Baeyens, G. Mazza, Comparing ANSYS Fluent ® and OpenFOAM ® simulations of Geldart A, B and D bubbling fluidized bed hydrodynamics, *Int. J. Numer. Meth. Heat Fluid Flow* 30 (2019) 93–118, <https://doi.org/10.1108/HFF-04-2019-0298>.
- [55] ENISO-4287, Geometrical Product Specifications (GPS)–Surface Texture: Profile Method–Terms, Definitions and Surface Texture Parameters (ISO 4287:1997), 1997.
- [56] KEPCO Inc., LC surface roughness measurements, 2020.
- [57] D. Geldart, J. Baeyens, The design of distributors for gas-fluidized beds, *Powder Technol.* 42 (1985) 67–78, [https://doi.org/10.1016/0032-5910\(85\)80039-5](https://doi.org/10.1016/0032-5910(85)80039-5).
- [58] B. Boissiere, R. Ansart, D. Gauthier, G. Flamant, M. Hemati, Experimental hydrodynamic study of gas-particle dense suspension upward flow for application as new heat transfer and storage fluid, *Can. J. Chem. Eng.* 93 (2015) 317–330, <https://doi.org/10.1002/cjce.22087>.
- [59] I. Cavarretta, C. O'Sullivan, M.R. Coop, M. Nakagawa, S. Luding, Applying 2D shape analysis techniques to granular materials with 3D particle geometries, in: *AIP Conf. Proc.*, AIP, 2009: pp. 833–836. 10.1063/1.3180057.
- [60] G.-C. Cho, J. Dodds, J.C. Santamarina, Particle shape effects on packing density, stiffness, and strength: natural and crushed sands, *J. Geotech. Geoenvironmental Eng.* 132 (2006) 591–602, [https://doi.org/10.1061/\(ASCE\)1090-0241\(2006\)132:5\(591\)](https://doi.org/10.1061/(ASCE)1090-0241(2006)132:5(591)).
- [61] S. Hovmand, J.F. Davidson, Chemical conversion in a slugging fluidised bed, *Trans. Inst. Chem. Eng.* 46 (1968) 190–203.
- [62] M.J. Rhodes, D. Geldart, The upward flow of gas/solid suspensions, Part 1, *Chem. Eng. Res. Des.* 67 (1989) 20–29.
- [63] H. Kqnnno, S. Saito, Pneumatic conveying of solids through straight pipes, *J. Chem. Eng. Japan* 2 (1969) 211–217, <https://doi.org/10.1252/jcej.2.211>.
- [64] Perry's chemical engineers' handbook, Choice Rev. Online. 35 (1998) 35-3079-35-3079. 10.5860/CHOICE.35-3079.
- [65] H. Littman, G.A.J. Homolka, The pressure field around a two-dimensional gas bubble in a fluidized bed, *Chem. Eng. Sci.* 28 (1973) 2231–2243, [https://doi.org/10.1016/0009-2509\(73\)85012-2](https://doi.org/10.1016/0009-2509(73)85012-2).
- [66] H.-Y. Xie, Pressure probes in the measurement of bubble properties in the fluidization of fine particles, *Adv. Powder Technol.* 8 (1997) 217–235, [https://doi.org/10.1016/S0921-8831\(08\)60464-1](https://doi.org/10.1016/S0921-8831(08)60464-1).
- [67] J.F. Davidson, D. Harrison, R. Jackson, Fluidized particles, *Chem. Eng. Sci.* 19 (1964) 701, [https://doi.org/10.1016/0009-2509\(64\)85059-4](https://doi.org/10.1016/0009-2509(64)85059-4).
- [68] H.L. Zhang, J. Degrevé, J. Baeyens, R. Dewil, Choking affects the operation diagram of a CFB riser, *J. Powder Technol.* 2014 (2014) 1–6, <https://doi.org/10.1155/2014/980416>.
- [69] M. Leva, *Fluidization* 1959, New York McGraw-Hill B. Ca). 329 (n.d.) 54.
- [70] H. Neau, M. Pigou, P. Fede, R. Ansart, C. Baudry, N. Mériçoux, J. Laviéville, Y. Fournier, N. Renon, O. Simonin, Massively parallel numerical simulation using up to 36,000 CPU cores of an industrial-scale polydispersed reactive pressurized fluidized bed with a mesh of one billion cells, *Powder Technol.* 366 (2020) 906–924, <https://doi.org/10.1016/j.powtec.2020.03.010>.
- [71] M.A. van der Hoef, M. van Sint Annaland, N.G. Deen, J.A.M. Kuipers, Numerical simulation of dense gas-solid fluidized beds: a multiscale modeling strategy, *Annu. Rev. Fluid Mech.* 40 (2008) 47–70, <https://doi.org/10.1146/annurev.fluid.40.111406.102130>.
- [72] J. Wang, M.A. van der Hoef, J.A.M. Kuipers, Why the two-fluid model fails to predict the bed expansion characteristics of Geldart A particles in gas-fluidized beds: a tentative answer, *Chem. Eng. Sci.* 64 (2009) 622–625, <https://doi.org/10.1016/j.ces.2008.09.028>.
- [73] K. Agrawal, P.N. Loezos, M. Syamlal, S. Sundaresan, The role of meso-scale structures in rapid gas–solid flows, *J. Fluid Mech.* 445 (2001) 151–185, <https://doi.org/10.1017/S0022112001005663>.
- [74] Y. Igci, A.T. Andrews, S. Sundaresan, S. Pannala, T. O'Brien, Filtered two-fluid models for fluidized gas-particle suspensions, *AIChE J.* 54 (2008) 1431–1448, <https://doi.org/10.1002/aic.11481>.

- [75] B.G.M. Van Wachem, J.C. Schouten, C.M. Van den Bleek, R. Krishna, J.L. Sinclair, Comparative analysis of CFD models of dense gas-solid systems, *AIChE J.* 47 (2001) 1035–1051, <https://doi.org/10.1002/aic.690470510>.
- [76] J.-F. Parmentier, O. Simonin, O. Delsart, A functional subgrid drift velocity model for filtered drag prediction in dense fluidized bed, *AIChE J.* 58 (2012) 1084–1098, <https://doi.org/10.1002/aic.12647>.
- [77] T. McKeen, T. Pugsley, Simulation and experimental validation of a freely bubbling bed of FCC catalyst, *Powder Technol.* 129 (2003) 139–152, [https://doi.org/10.1016/S0032-5910\(02\)00294-2](https://doi.org/10.1016/S0032-5910(02)00294-2).
- [78] J. Wang, A review of eulerian simulation of geldart a particles in gas-fluidized beds, *Ind. Eng. Chem. Res.* 48 (2009) 5567–5577, <https://doi.org/10.1021/ie900247t>.
- [79] J. Li, Particle-fluid two-phase flow: the energy-minimization multi-scale method, Metallurgical Industry Press, 1994.
- [80] J. Li, M. Kwauk, Exploring complex systems in chemical engineering—the multi-scale methodology, *Chem. Eng. Sci.* 58 (2003) 521–535, [https://doi.org/10.1016/S0009-2509\(02\)00577-8](https://doi.org/10.1016/S0009-2509(02)00577-8).
- [81] W. Wang, J. Li, Simulation of gas-solid two-phase flow by a multi-scale CFD approach—of the EMMS model to the sub-grid level, *Chem. Eng. Sci.* 62 (2007) 208–231, <https://doi.org/10.1016/j.ces.2006.08.017>.
- [82] H. Luo, B. Lu, J. Zhang, H. Wu, W. Wang, A grid-independent EMMS/bubbling drag model for bubbling and turbulent fluidization, *Chem. Eng. J.* 326 (2017) 47–57, <https://doi.org/10.1016/j.cej.2017.04.145>.
- [83] W. Wang, B. Lu, J. Geng, F. Li, Mesoscale drag modeling: a critical review, *Curr. Opin. Chem. Eng.* 29 (2020) 96–103, <https://doi.org/10.1016/j.coche.2020.07.001>.
- [84] Z. Shi, W. Wang, J. Li, A bubble-based EMMS model for gas-solid bubbling fluidization, *Chem. Eng. Sci.* 66 (2011) 5541–5555, <https://doi.org/10.1016/j.ces.2011.07.020>.
- [85] K. Hong, Z. Shi, W. Wang, J. Li, A structure-dependent multi-fluid model (SFM) for heterogeneous gas-solid flow, *Chem. Eng. Sci.* 99 (2013) 191–202, <https://doi.org/10.1016/j.ces.2013.05.050>.
- [86] A. Ozel, P. Fede, O. Simonin, Development of filtered Euler-Euler two-phase model for circulating fluidized bed: High resolution simulation, formulation and a priori analyses, *Int. J. Multiph. Flow* 55 (2013) 43–63, <https://doi.org/10.1016/j.ijmultiphaseflow.2013.04.002>.
- [87] C.C. Milioli, F.E. Milioli, W. Holloway, K. Agrawal, S. Sundaresan, Filtered two-fluid models of fluidized gas-particle flows: New constitutive relations, *AIChE J.* 59 (2013) 3265–3275, <https://doi.org/10.1002/aic.14130>.
- [88] A. Sarkar, F.E. Milioli, S. Ozarkar, T. Li, X. Sun, S. Sundaresan, Filtered sub-grid constitutive models for fluidized gas-particle flows constructed from 3-D simulations, *Chem. Eng. Sci.* 152 (2016) 443–456, <https://doi.org/10.1016/j.ces.2016.06.023>.
- [89] S. Schneiderbauer, A spatially-averaged two-fluid model for dense large-scale gas-solid flows, *AIChE J.* 63 (2017) 3544–3562, <https://doi.org/10.1002/aic.15684>.
- [90] J.H. Cloete, S. Cloete, F. Munichi, S. Radl, S. Amini, Development and verification of anisotropic drag closures for filtered Two Fluid Models, *Chem. Eng. Sci.* 192 (2018) 930–954, <https://doi.org/10.1016/j.ces.2018.06.041>.
- [91] J.H. Cloete, S. Cloete, S. Radl, S. Amini, Development and verification of anisotropic solids stress closures for filtered Two Fluid Models, *Chem. Eng. Sci.* 192 (2018) 906–929, <https://doi.org/10.1016/j.ces.2018.06.040>.
- [92] A. Boelle, G. Balzer, O. Simonin, Second-order prediction of the particle-phase stress tensor of inelastic spheres in simple shear dense suspensions, in: *Am. Soc. Mech. Eng. Fluids Eng. Div. FED*, 1995.
- [93] A. Srivastava, S. Sundaresan, Analysis of a frictional-kinetic model for gas-particle flow, *Powder Technol.* 129 (2003) 72–85, [https://doi.org/10.1016/S0032-5910\(02\)00132-8](https://doi.org/10.1016/S0032-5910(02)00132-8).
- [94] C.Y. Wen, Y.H. Yu, A generalized method for predicting the minimum fluidization velocity, *AIChE J.* (1966), <https://doi.org/10.1002/aic.690120343>.
- [95] A. Gobin, H. Neau, O. Simonin, J.-R. Llinas, V. Reiling, J.-L. Sélo, Fluid dynamic numerical simulation of a gas phase polymerization reactor, *Int. J. Numer. Meth. Fluids* 43 (2003) 1199–1220, <https://doi.org/10.1002/fld.542>.
- [96] O. Simonin, S. Chevrier, F. Audard, P. Fede, Drag force modelling in dilute to dense particle-laden flows with mono-disperse or binary mixture of solid particles, *Proc. 9th Int. Conf. Multiph. Flow* (2016).
- [97] R. Ansart, P. García-Triñanes, B. Boissière, H. Benoit, J.P.K. Seville, O. Simonin, Dense gas-particle suspension upward flow used as heat transfer fluid in solar receiver: PEPT experiments and 3D numerical simulations, *Powder Technol.* 307 (2017) 25–36, <https://doi.org/10.1016/j.powtec.2016.11.006>.
- [98] H. Benoit, R. Ansart, H. Neau, P. Garcia Triñanes, G. Flamant, O. Simonin, Three-dimensional numerical simulation of upflow bubbling fluidized bed in opaque tube under high flux solar heating, *AIChE J.* 64 (2018) 3857–3867, <https://doi.org/10.1002/aic.16218>.
- [99] G. Zhao, X. Shi, Y. Wu, M. Wang, M. Zhang, J. Gao, X. Lan, 3D CFD simulation of gas-solids hydrodynamics and bubbles behaviors in empty and packed bubbling fluidized beds, *Powder Technol.* 351 (2019) 1–15, <https://doi.org/10.1016/j.powtec.2019.04.003>.
- [100] V. Verma, J.T. Padding, N.G. Deen, J.A.M.H. Kuipers, F. Barthel, M. Bieberle, M. Wagner, U. Hampel, Bubble dynamics in a 3-D gas-solid fluidized bed using ultrafast electron beam X-ray tomography and two-fluid model, *AIChE J.* 60 (2014) 1632–1644, <https://doi.org/10.1002/aic.14393>.
- [101] J. Baeyens, S.Y. Wu, Bed expansion and the visible bubble flow rate in gas fluidized beds, *Adv. Powder Technol.* 3 (1992) 163–189, [https://doi.org/10.1016/S0921-8831\(08\)60668-8](https://doi.org/10.1016/S0921-8831(08)60668-8).
- [102] A. Chen, H.T. Bi, Pressure fluctuations and transition from bubbling to turbulent fluidization, *Powder Technol.* 133 (2003) 237–246, [https://doi.org/10.1016/S0032-5910\(03\)00119-0](https://doi.org/10.1016/S0032-5910(03)00119-0).
- [103] A. Stefanova, H.T. Bi, C.J. Lim, J.R. Grace, Heat transfer from immersed vertical tube in a fluidized bed of group A particles near the transition to the turbulent fluidization flow regime, *Int. J. Heat Mass Transf.* 51 (2008) 2020–2028, <https://doi.org/10.1016/j.ijheatmasstransfer.2007.06.005>.
- [104] A. Stefanova, X.T. Bi, C.J. Lim, J.R. Grace, A probabilistic heat transfer model for turbulent fluidized beds, *Powder Technol.* 365 (2020) 163–171, <https://doi.org/10.1016/j.powtec.2019.01.066>.